The Pennsylvania State University

The Graduate School

John and Willie Leone Family Department of Energy and Mineral Engineering

AN IMPROVED METHOD OF PERMEABILITY ESTIMATION BASED ON

PULSE-DECAY EXPERIMENT USING ILLINOIS COAL

A Thesis in

Energy and Mineral Engineering

by

Zhicheng Fang

Submitted in Partial Fulfillment
of the Requirements
for the Degree of

Master of Science

August 2017

The thesis of Zhicheng Fang was reviewed and approved* by the following:

Shimin Liu
Assistant Professor of Energy and Mineral Engineering
Thesis Advisor

Chaopeng Shen
Assistant Professor of Civil Engineering

Turgay Ertekin
Professor of Petroleum and Natural Gas Engineering

Sanjay Srinivasan
Professor of Petroleum and Natural Gas Engineering
Head, John and Willie Leone Family Department of Energy and Mineral
Engineering

*Signatures are on file in the Graduate School

ABSTRACT

For tight unconventional gas reservoir formations, such as shale or coal, the transient 'pulse-decay' technique is a time-effective method to experimentally estimate the rock permeability from the pressure versus time profile data. Currently the analytical solution of permeability that is derived based on the expression of simulated pressure profile has been widely used (Cui et al., 2009). However, this solution may lead to erroneous results because the assumption of constant gas properties is not always valid. Besides, the permeability solution is obtained by making simulated pressure profile and experimental pressure curve have the same late-time slope. In some cases, however, different pressure decay characteristics are observed demonstrating the huge differences between simulated and experimental pressure profiles and the invalidity of the permeability result. To overcome these limitations, in this study a new method of permeability measurement is designed. Finite difference method is used to solve the governing equation numerically and reproduce the experimental pressure profile. Pressure-dependent gas properties are incorporated in numerical simulation, and permeability is obtained when the differences between simulated and experimental pressure profiles are minimum. The minimum differences ensure similar pressure decay characteristics and can be quantified by the history-matching method. This new approach was tested by measuring permeability from pulse-decay experiments conducted on Illinois coal; the types of tested gases included helium, methane and carbon dioxide. The results show improved permeability values compared with the analytical solutions of Cui et al. (2009). Two factors contained in this proposed numerical approach result in the improvement: (1) be able to apply pressure-dependent gas properties; (2) using the whole pressure profile to capture the pressure decay dynamics so that improved gas permeability estimation can be provided. Finally, sensitivity analysis is carried out. It is found that the second factor is more influential in determining permeability in this study, and the numerically estimated permeability is not sensitive to porosity,

Langmuir pressure and Langmuir volume, which is an advantage for the reliable permeability estimation through the pulse-decay technique.

TABLE OF CONTENTS

LIST OF FIGURES

LIST OF TABLES

ACKNOWLEDGEMENTS

Chapter 1

Introduction

Coalbed methane (CBM) is an important natural gas resource in the United States. Figure 1-1 shows the production of CBM from 1989 to 2014. The production increased from 1989 to 2008 and accounted for about 9% of total natural gas production in 2008. After 2008, CBM production slightly decreased because of a reduction in new CBM well drilling; however, it still takes up over 5% of total natural gas production and remains an important part of produced gas. In the U.S., Illinois coal is one of the main contributors to coal production and contains a significant amount of gas resources demonstrating its exploitation potential. For CBM exploitation, permeability is an important parameter that determines the production potential and ultimate recovery of the gas resources (Chen et al., 2015); therefore, a sound knowledge of permeability is required for CBM reservoir evaluation. However, accurate coal permeability estimation is quite challenging because the gas transport is a multimechanical process. Due to complex and tight pore structures, different flow regimes may co-exist in coal; these include viscous flow, Knudsen diffusion, slip flow, and sorption (Javadpour, 2009). If only conventional Darcy's flow is considered, the permeability will be underestimated (Cui et al., 2009). Also, it is experimentally challenging to directly apply the traditional steady-state method to estimate the permeability because it may take an extremely long time to achieve steady-state flow (Hsieh et al., 1981), and small flow rates cannot be measured with sufficient accuracy (Finsterle and Persoff, 1997). If large volumes of fluids are applied during the traditional measurement process, damage to the tight rocks will be readily induced (Amaefule et al., 1986).
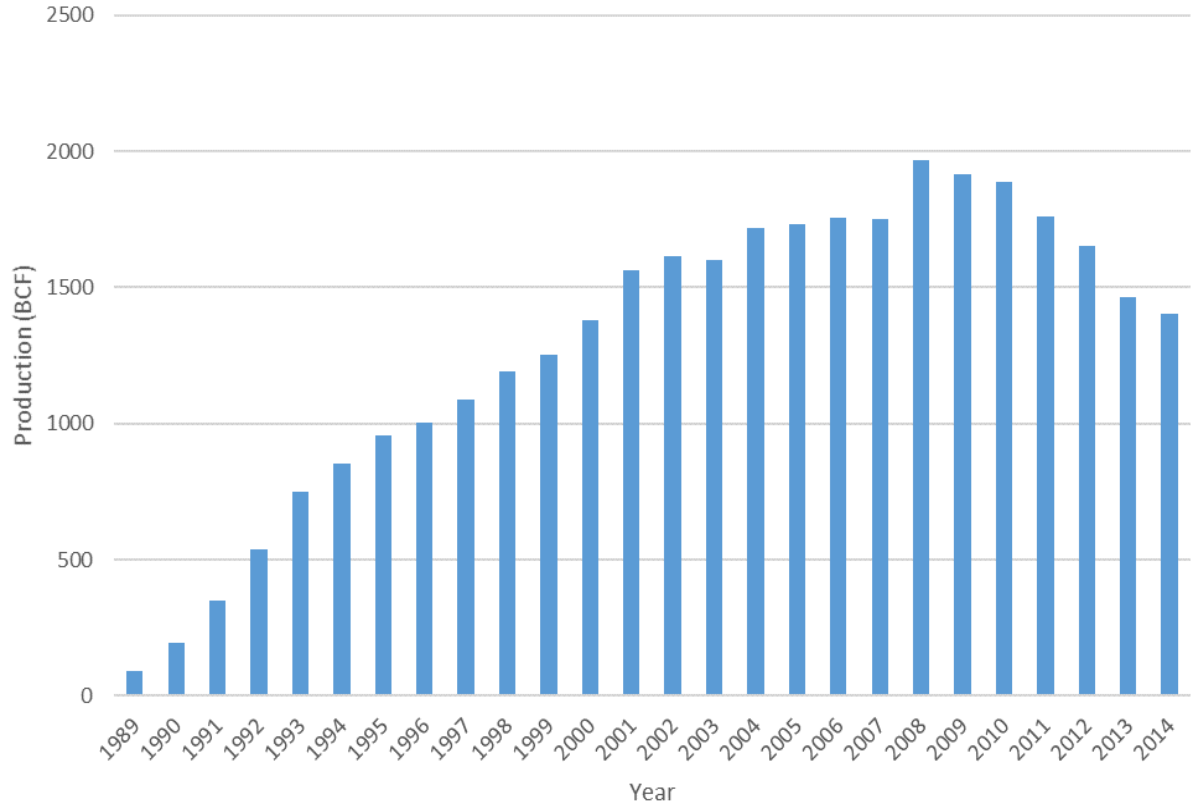
Figure 1-1 Coalbed Methane Production (EIA, 2015)

Alternatively, the transient 'pulse-decay' technique is often employed. This method enables permeability measurement of tight rocks, which can be as low as 10^{-15} m^2. Noting that permeability is the only unknown parameter to be determined based on the experimental pressure decay data (Brace et al., 1968), proper pressure curve analysis and interpretation are required to accurately estimate the permeability.

Extensive efforts have been made toward pulse-decay permeability determination (Brace et al., 1968; Yamada and Jones, 1980; Hsieh et al., 1981; Bourbie and Walls, 1982; Dicker and Smits, 1988; Cui et al., 2009). Cui et al. (2009) proposed an analytical solution to determine the gas permeability for both sorptive and non-sorptive gases, and their proposal was widely applied. In Cui et al.'s method, gas properties are assumed to be constant, and based on the expression of simulated pressure profile, the analytical solution of permeability is obtained by the late-time

technique (Cui et al., 2009). However, this estimation method have two drawbacks that need to be fixed: (1) the assumption of constant gas properties may not be valid under certain conditions (Darabi et al., 2012)**;** (2) permeability obtained by the late-time technique may not be representative since significant differences between simulated and experimental pressure profiles may exist although their late-time slopes are satisfactorily similar. This is in contrast to the ultimate goal that the desired permeability corresponds to simulated pressure data which can reproduce the entire experimental pressure profile. Therefore, a reliable method of permeability estimation based on pulse-decay data is still needed to assist the development of tight reservoir rock permeability estimation that can be widely applied. In this study, a new numerical approach is proposed to overcome the limitations already mentioned. In the proposed approach, the pulse-decay pressure profiles are numerically estimated with the assumed permeability. This numerical estimation can dynamically evaluate the values of different gas properties. Then, based on the pressure history-matching results, the permeability at each pressure step is determined when the measured and numerically modeled pressure data are well matched. This proposed approach was employed to estimate the permeability of Illinois coal through pulse-decay experiments. Helium, methane, and carbon dioxide (CO_2) are used as the tested fluids. Improved permeability results are shown compared with the analytical solutions of Cui et al. (2009). Such improvement can be attributed to the adoption of pressure-dependent properties rather than constant properties, and the history-matching method instead of the late-time technique to determine permeability. Sensitivity analysis isolates the effect of each factor and shows that history-matching method is more crucial for permeability results while pressure-dependent properties impose little influence on permeability results. Finally, pressure decay characteristics are shown to change little with the variation of porosity, Langmuir pressure or Langmuir volume, which illustrates that permeability results are expected to remain at a constant value as assumed porosity, Langmuir pressure or Langmuir volume varies.

Chapter 2

Background and Literature Review

2.1 Background of Illinois Basin Coal Geology

Illinois coal, as the name indicates, is the coal found in the Illinois Basin, which covers 65% of Illinois and portions of southwestern Indiana and western Kentucky. According to the classification standards, Illinois coal belongs to bituminous thermal coal, which is used in cement plants, electric power generation, and other industrial fields. In the state of Illinois, the total amount of recoverable coal reserves is estimated to be 30 billion tons, which accounts for 12.5% of the total coal reserves and 25% of the bituminous coal reserves. In 2013, Illinois ranked second in recoverable coal reserves at producing mines. Because of the abundance of Illinois coal, it has become a major part of the Illinois economy and it ranks third in coal production following the Powder River Basin of Wyoming and Montana and the Appalachian Basin. Although the methane content of Illinois coal is small, the total amount of methane resources is huge because of numerous coal resources (Damberger and Demir, 1999). Potential gas resources in the Illinois Basin are estimated to be 21 Tcf (Tedesco et al., 2003).

Coalbed methane exploitation in Illinois coal started in the mid-1980s. For the first fifteen years, only small amount of gas was produced from numerous abandoned mines, and there were some attempts to make coalbed methane productive and profitable. Rodvelt and Oestreich (2005) set up a resource evaluation plan to make field development successful, and Morse and Demir (2007) generated additional gas production data through the drilling of new wells. Because of positive factors such as multiple coal seams and strong gas markets, the future of coalbed methane in the Illinois Basin is still promising, and significant investment is expected for its development.

2.2 Gas Flow in Coal and Permeability

2.2.1 Flow Mechanisms in Coal

The gas flow mechanisms in coal are complex and involve several processes. During a typical production process, water is produced initially because the cleats are filled with water (Aminian, 2007). As water is produced continuously, free gas is also released and reservoir pressure decreases. When 'critical desorption pressure' is reached, gas desorbs from the matrix surface and flows into the cleat system. As free gas accumulates in the cleat system, gas saturation increases and gas flows toward the production well when the gas saturation exceeds critical gas saturation. At the same time, gas desorption from the matrix surface forms the concentration gradient, inducing gas diffusion within the matrix.

Generally, free gas flows, gas desorbs, and gas diffuses through the matrix. These processes may overlap (Javadpour et al., 2007**;** Javadpour, 2009). Therefore, gas flow in coal is usually a combination of several flow mechanisms including gas sorption, molecular diffusion, advection, and Knudsen/slip flow (Alharthy et al., 2012).

2.2.2 Apparent Permeability

Because of the complexity of nanoscale flow, traditional Darcy's flow with intrinsic permeability cannot represent gas transport inside, and production from these strata is usually much higher than expected. Therefore, the concept of 'apparent permeability' is introduced to quantify the flow enhancement (Javadpour, 2009). Its expression varies depending on the flow mechanisms considered. To quantify the permeability enhancement induced by gas slippage, Klinkenberg (1941) first introduced the equation used to correct for permeability, as shown in equation 2-1:

$$k_a = k_\infty(1 + \frac{b_k}{\bar{P}})$$

<div align="right">Equation 2-1</div>

where, k_a is the apparent permeability, k_∞ is the intrinsic/Darcy permeability, $\bar{P}$ is the mean pore pressure, and b_k is the Klinkenberg factor which can be expressed with equation 2-2 (Randolph et al., 1984; Wang et al., 2015):

$$b_k = \frac{16c\mu}{w}\sqrt{\frac{2RT}{\pi M}}$$

<div align="right">Equation 2-2</div>

where, c is the constant typically taken as 0.9, μ is viscosity, M is the molecular weight, w is the width of the pore throat, R is the universal gas constant, and T is temperature.

According to the derivation of Klinkenberg (1941), $\frac{b_k}{\bar{P}}$ can be described as:

$$\frac{b_k}{\bar{P}} = \frac{4c\bar{\lambda}}{r}$$

<div align="right">Equation 2-3</div>

where, c is a proportionality factor constant at 1.0, and r is the mean radius of the pores. $\bar{\lambda}$ is the mean free path of gas molecules which are expressed as follows:

$$\lambda = \frac{k_B T}{\sqrt{2}\pi\delta^2 P}$$

<div align="right">Equation 2-4</div>

where, k_B is the Boltzmann constant ($1.3805*10^{-23}$J/K), T is the temperature, P is pressure and δ is the collision diameter of the gas molecule.

From equation 2-1 and equation 2-3, Klinkenberg (1941) concluded that apparent permeability does not depend on the pressure difference *(P₁-P₂)* and it varies for different types of gases since the mean free path $\bar{\lambda}$ has different values in this case. Moreover, the apparent

permeability extrapolated to infinite pressure ($\frac{1}{P} = 0$) is the true permeability, which only depends on the characteristics of the porous medium.

However, the equation of Klinkenberg (1941) eliminated the kinetic effect the rebounding molecules could have on the fluid flow in smaller capillaries (Fathi et al., 2012). According to the theory of Fathi et al. (2012), both the molecules interacting with the capillary wall and those interacting with bulk fluid slip. The double-slip effect gives the modified Klinkenberg equation:

$$k_a = k[1 + \left(\frac{b_k}{p}\right)^2 (\frac{L_{Ke}}{\lambda})]$$

Equation 2-5

where, L_{Ke} is a new length scale related to the rebounding molecules' kinetic energy.

By taking Knudsen diffusion and slip flow into account and taking the form of Darcy's law, Javadpour (2009) put forward another equation of apparent permeability:

$$k_{app} = \frac{2r\mu M}{3 * 10^3 RT \rho_{avg}^2} (\frac{8RT}{\pi M})^{0.5} + F\frac{r^2}{8\rho_{avg}}$$

Equation 2-6

where, r is pore radius, μ is viscosity, M is molecular weight, R is gas constant, T is temperature, ρ_{avg} is average density, and F is introduced by Brown et al. (1946) to correct for slip velocity:

$$F = 1 + \left(\frac{8\pi RT}{\pi M}\right)^{0.5} \frac{\mu}{P_{avg}r} (\frac{2}{\alpha} - 1)$$

Equation 2-7

where, α varies from 0 to 1 depending on wall surface smoothness, gas type, temperature, and pressure. The ratio of apparent permeability to intrinsic permeability shows that apparent permeability is always higher than intrinsic permeability. Depending on pressure, pore size, or other factors, the extent of permeability enhancement varies. At smaller pores and lower pressures, the enhancement is larger. However, temperature and gas molar mass have the minimal effects on permeability enhancement.

To make apparent permeability easily applied to the commercial reservoir simulator, gas flow is written in the form of the Darcy equation (Javadpour, 2009) with apparent permeability applied. Jiang and Younis (2015) established multi-continuum numerical simulator incorporating the 'apparent permeability' term into the governing equation to conduct fractured reservoir simulation, which proved to be useful. In this study, the value of apparent permeability can be estimated by analyzing pulse-decay data and the method of estimating apparent permeability will be introduced in detail in 2.4.

2.2.3 Sorption Effect on Permeability

As a primary storage mechanism in coal (Aminian, 2007), sorption has a non-negligible effect on gas flow. It influences coal permeability by generating coal volumetric variations. Generally, coal shrinks when gas desorbs and swells when gas adsorbs onto the matrix surface. Due to the volumetric change effect, in the field of CO_2 sequestration for enhanced recovery, permeability behavior can be complex since injected gas may adsorb to the surface leading to matrix swelling and permeability reduction, which can be harmful to production (Shi and Durucan, 2005). The relationship between swelling strain and the amount of adsorbed gas can be linear (Levine, 1996; Czerw, 2011; Wang et al., 2011) or non-linear (Day et al., 2008; Kelemen and Kwiatek, 2009; Wang et al., 2011). To evaluate their relationship, Palmer and Mansoori (1998) gave the permeability equation expressed as a function of effective stress and matrix shrinkage under uniaxial strain conditions which are usually expected in a reservoir. Pan and Connell (2007) derived the P&C model to quantify adsorption-induced coal swelling using an energy balance approach which assumes that the change in surface energy caused by adsorption is equal to the coal solid's elastic energy change. To model with fewer input parameters compared with Pan and Connell (2007) and reduce the relevant uncertainties, Liu and Harpalani (2013a) proposed another

model to quantify the volumetric changes of the coal matrix under the additive effects of gas sorption and mechanical compression. This strain model can be coupled into the permeability prediction model to evaluate permeability evolution during primary depletion (Liu and Harpalani, 2013b). All of these models enhance the understanding of sorption-induced coal volumetric change and stress the importance of the sorption effect on permeability determination. Therefore, it cannot be ignored to ensure comprehensive interpretation.

2.3 Pulse-Decay Techniques

In this study, a transient pulse-decay experiment is conducted to estimate coal permeability. This method enables permeability measurement as low as 10^{-15} m^2 (1mD=10^{-15} m^2). Figure 2-1 shows a typical layout of the experiment. Initially, the pressure over the whole system is in equilibrium and the main valve is closed. Then upstream pressure is increased and the main valve is opened, which forms the driving force for the gas to flow throughout the whole system. During the process of gas flow, pressure transducers are used to record the pressure variations of upstream and downstream vessels. When the pressure equilibrates again in the system, the experiment ends and the resulting upstream and downstream pressure profiles are used for permeability determination.

There is extensive study on pulse-decay data interpretation. A popular method is that the analytical solution of the pressure profile can be put forward based on the governing equation describing gas flow in tight rocks. By comparing the simulated pressure solution with experimental pressure data, the analytical solution of permeability can be put forward. Brace et al. (1968) first derived the equation to calculate permeability with the assumption of no compressive storage and no sorption effect. However, the assumption of zero compressive storage is not valid and may induce significant errors (Lin, 1977; Yamada and Jones, 1980; Bourbie and Walls, 1982; Metwally

and Sondergeld, 2011). Bourbie and Walls (1982) showed that the margin of error from Brace et al. (1968) may be as high as 25% or larger. Dicker and Smits (1988) proposed an improved permeability equation by taking compressive storage into account. However, this method ignores the sorption effect on the permeability result. Cui et al. (2009) improved the analytical solution by adding a sorption term to the governing equation and introduced different governing equations corresponding to different shapes of the specimens. This can be regarded as a comprehensive interpretation and the resulting permeability equation is shown as:

$$k = \frac{-s_1 \mu c_g L}{f_1 A(\frac{1}{V_u} + \frac{1}{V_d})}$$

<div align="right">Equation 2-8</div>

where, s_1 is the semi-log slope of differential pressure (pressure difference between upstream pressure and downstream pressure), μ is viscosity, c_g is gas compressibility, L is the specimen length, A is cross-sectional area of the specimen, V_u and V_d are the upstream volume and downstream volume, respectively, and f_1 is the factor used to correct for mass flow (Jones, 1997):

$$f_1 = \frac{\theta_1^2}{a + b}$$

<div align="right">Equation 2-9</div>

where, θ_1 is the first root of the equation below:

$$tan\theta = \frac{(a + b)\theta}{\theta^2 - ab}$$

<div align="right">Equation 2-10</div>

where, a is the ratio of pore volume V_p to upstream volume V_u and b is the ratio of pore volume V_p to downstream volume V_d:

$$a = \frac{V_P}{V_u}$$

<div align="right">Equation 2-11</div>

$$b = \frac{V_P}{V_d}$$

<div align="right">Equation 2-12</div>

For adsorptive gas like methane and carbon dioxide, the storage capacity of the specimen becomes:

$$a = \frac{V_p(1 + \frac{\phi_a}{\phi})}{V_u}$$

<div align="right">Equation 2-13</div>

$$b = \frac{V_p(1 + \frac{\phi_a}{\phi})}{V_d}$$

<div align="right">Equation 2-14</div>

where, ϕ is the true porosity of the specimen and ϕ_a is defined as the effective adsorption porosity:

$$\phi_a = \frac{\rho_s}{V_{std}} * \frac{(1 - \phi)}{c_g \rho} * \frac{q_L P_L}{(P_L + P)^2}$$

<div align="right">Equation 2-15</div>

where, ρ_s is skeleton density of the specimen, V_{std} is mole volume of gas at standard temperature (273.15K) and pressure (101325Pa), ρ is gas density, P is pressure, q_L and P_L are Langmuir volume and pressure, respectively. c_g is gas compressibility expressed as:

$$c_g = \frac{1}{\rho}\frac{d\rho}{dP} = \frac{1}{P} - \frac{1}{Z}\frac{dZ}{dP}$$

<div align="right">Equation 2-16</div>

The method of Cui et al. (2009) is based on the assumption that gas density ρ, viscosity μ, and gas compressibility c_g are constant. However, according to Darabi et al., (2012), the assumption of constant gas properties is not always valid. When the pressure difference across the specimen is large or the initial pressure is low, the analytical solution may lead to a significant error. Therefore, pressure-dependent properties need to be implemented in permeability prediction.

Furthermore, to get the analytical solution of Cui et al. (2009), the slope of the semi-log curve at late time is taken as term s_l in equation 2-8. However, considering the experimental conditions and complexity of flow mechanisms, the trends that experimental curves and pressure solutions follow may not be strictly the same so that only matching the slope at late time may induce huge discrepancies between simulated and experimental pressure profiles, which is antithetical to the goal that they should be as close as possible. Figure 2-2 shows the comparison of differential pressure dP_d (defined in equation 2-17) for CO_2 at the 6th pressure step in this study. From this figure it can be observed that although the late-time slope is satisfactorily similar, during the early time period (10-40s) significant variations raise concerns about the accuracy of the analytical solution of permeability. This huge difference needs to be minimized as much as possible because the governing equation applies to the whole experimental process.

$$dP_d(t) = \frac{P_u(t) - P_d(t)}{P_u(0) - P_d(0)}$$

Equation 2-17
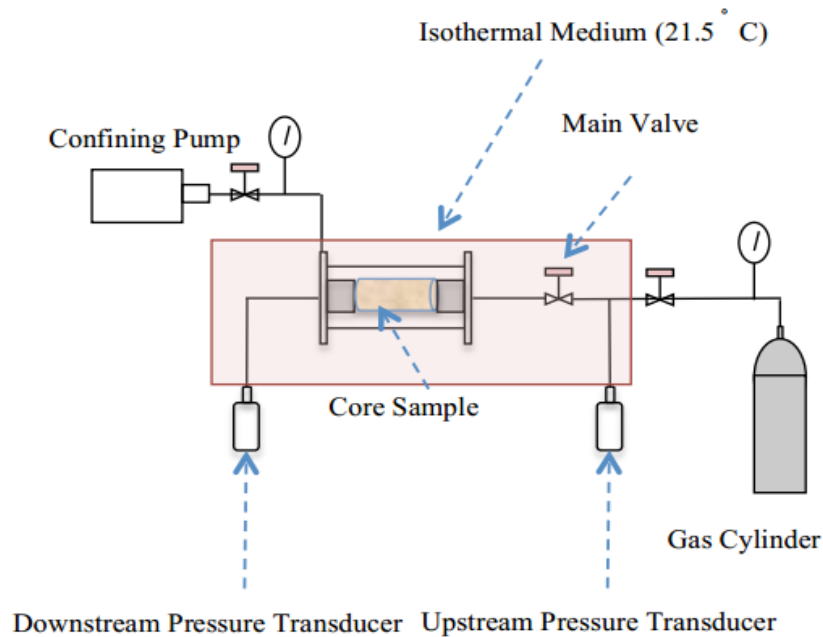
Figure 2-1 Layout of Pulse-Decay Experiments (Alnoaimi and Kovscek, 2013)
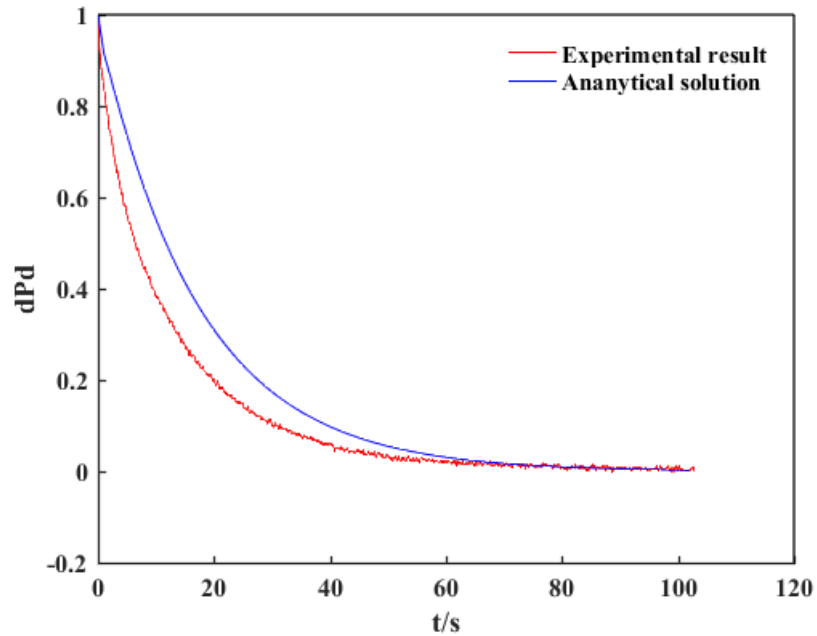
Figure 2-2 Comparison of Differential Pressure Obtained by the Experiment and Analytical Solution

To get the best fit between pressure profiles, history-matching method is introduced. It involves an inverse problem of obtaining unknown properties by matching simulation results to the observed data as closely as possible (Dos Santos Amorim et al., 2010). Haskett et al. (1988) applied the analytical solution to history-match the measured pressure data and verified the validity of the analytical solution by comparing it with the numerical simulator. However, this method does not apply to adsorptive gas. Alnoaimi and Kovscek (2013) used the history-matching method to investigate the gas permeability of Eagle Ford shale cores. However, the governing equation refers to 2-D flow and cannot be applied directly to this study. Moreover, compared with the analytical solution of Cui et al. (2009), this method requires additional properties such as pressure-dependent gas formation volume factor B_g, making the permeability measurement more complex.

In this study, pulse-decay experiments were conducted on Illinois coal. The types of gases tested included helium, methane, and carbon dioxide. For each type of gas, six increasing pressure

steps are performed; this can be achieved by the gas injection process. During the experiment, constant stress boundary condition is used, which means that axial and confining stresses are kept constant. After obtaining the experimental results, a new method which combines numerical simulation with the history-matching method is introduced to measure permeability. This method does not require additional parameters compared with the analytical solution of Cui et al. (2009), and ensures dynamic evaluation of gas properties and the best fit between simulated and experimental pressure profiles, which can be regarded as an improvement of the analytical solution of Cui et al. (2009).

Chapter 3

Methodology

In this part a general procedure for the new approach of permeability estimation is described. It is mainly divided into three parts: the first part is experimental investigation. The second part is numerical simulation. The governing equation with the assumption of pressure-dependent gas properties are put forward and finite difference method is used to solve the governing equation and reproduce the upstream and downstream pressure profile. MATLAB code is used for simulation. The third part is history matching. To evaluate the matching extent between experimental and simulation results, the objective function is defined and the desired permeability corresponds to the minimum objective function. To investigate the effect of pressure-dependent properties on the permeability results, the governing equation with the assumption of constant gas properties is also numerically solved and the procedure of numerical simulation is detailed in part 3.2.2.

3.1 Experimental Work

3.1.1 Specimen Preparation

Blocks of Illinois coal were obtained from the Illinois Basin. Cylindrical specimens with 1 inch in diameter were drilled from the blocks, and they were trimmed to ~2-inches in length. Then all the specimens were dried for 24 hours to evacuate the moisture. Before the experiment, specimens were preserved in the plastic sample bag to ensure their integrity.

3.1.2 Experimental Setup

Figure 3-1 shows the layout of the experimental apparatus, which is the same as the facility shown by Wang et al. (2015). V1 to V4 refers to different valves. V1 is used to control gas flow into the specimen, and V2 is used to control gas flow into the downstream reservoir. V3 and V4 control the confining stress and axial stress loaded on the specimen, respectively. With the help of the desktop LabVIEW control panel, stress can be maintained or controlled by the syringe pumps. The specimen, which is covered with aluminum foil, is placed inside the rubber jacket and the rubber jacket is put into the center of the triaxial cell. The aluminum foil is used to avoid contact between the specimen and the rubber jacket; the rubber jacket is used to isolate the specimen from the confining fluid. Upstream and downstream reservoirs are placed at two sides of the specimen, and the gas cylinder is capable of generating additional pressure in the upstream reservoir if necessary. Two USB-based Omega pressure transducers were installed to record pressure variations in the upstream and downstream vessels. During the experimental process, the temperature was kept constant at 23°C (296 K), and the resulting pressure profile could be used to estimate permeability.
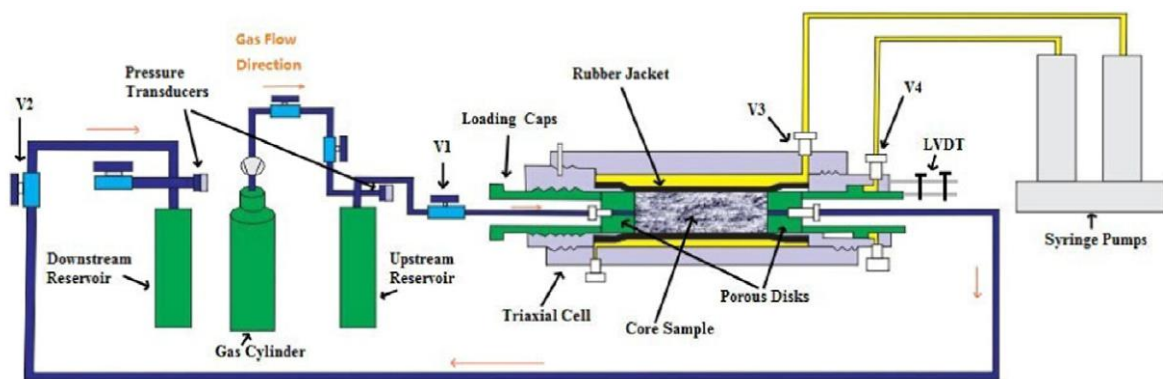
Figure 3-1 Arrangement of Experimental Apparatus (Wang et al., 2015)

3.1.3 Experimental Procedure

In this study, the specimen permeability to helium, methane, and carbon dioxide was measured under constant stress boundary condition. Permeability evolution was investigated during the process of gas injection. As a non-sorbing gas, helium permeability was tested first. The confining stress was gradually loaded to 1000 psi, and the axial stress was gradually loaded to 696 psi. The vacuum pump could be applied to remove residual air from the experimental apparatus. Helium was injected into both the upstream and downstream vessels at 14 psi, and after equilibrium was reached, upstream pressure was increased to 31 psi by continuing to inject gas into the upstream reservoir. This formed the driving force for gas to flow, and the valve which isolated the upstream vessel from the triaxial cell and downstream vessel (V1) was opened to let gas flow through the system. The experiment ended when the whole system reached final equilibrium. Based on the recorded pressure variations, permeability could be estimated. After the first pressure step was finished, upstream and downstream pressures were increased for the next pressure step. After reaching equilibrium, upstream pressure was increased by the value similar to the previous step (17 psi) so that gas started flowing. By repeating the procedures mentioned above, six increasing pressure steps were carried out and permeability evolution during this injection process could be evaluated. After the helium cycle, methane and carbon dioxide were used for permeability measurements following the same procedures mentioned above. Six pressure steps were conducted for each type of gas and the confining and axial stresses remained at 1000 psi and 696 psi, respectively.

3.2 Numerical Simulation

With the pulse-decay data, permeability of the tested coal can be estimated. I propose to use numerical method to replicate the pressure profiles for both downstream and upstream vessels because the governing equation includes pressure-dependent properties which are non-linear terms and cannot be solved analytically. To investigate the effect of pressure-dependent properties on the permeability results, numerical simulation is also used to solve the governing equation with constant gas properties. The detailed numerical procedure is shown below:

3.2.1 Numerical Simulation Using Constant Gas Properties

When gas properties including gas density (ρ), compressibility (c_g) and viscosity (μ) are constant and taken as a function of final equilibrium pressure at each pressure step, the governing equation describing pressure variations along the axis of the cylindrical sample is (Cui et al., 2009):

$$\frac{\partial P}{\partial t} = \frac{k}{\mu c_g(\phi + (1-\phi)K_a)} * \frac{\partial^2 P}{\partial x^2} \text{ for } 0 < x < L, t > 0$$

Equation 3-1

where, P is pressure, t is time, k is permeability, ϕ is porosity, x is displacement, L is sample length

and $K_a = \frac{\partial q}{\partial \rho} = \frac{\rho_s}{V_{std}} \frac{1}{c_g \rho} \frac{q_L P_L}{(P+P_L)^2}$ is defined as the derivative of adsorbate density q with respect to

the gas density ρ and it is taken as a function of final equilibrium pressure at each pressure step. The gas density ρ can be given by real gas law:

$$\rho = \frac{P}{ZRT}$$

Equation 3-2

where, Z is gas compressibility factor estimated by the Peng-Robinson equation of state, R is the universal gas constant, and T is temperature.

The initial condition is given below:

$$P(r, 0) = P_d(0) \text{ for } 0 < r < L$$

Equation 3-3

Initially, pressure along the specimen is equal to the initial downstream pressure. The corresponding boundary conditions are listed below:

$$P(0, t) = P_u(t) \text{ for } t \geq 0$$

Equation 3-4

$$P(L, t) = P_d(t) \text{ for } t \geq 0$$

Equation 3-5

$$\frac{kA}{\mu c_g} * \frac{dP}{dx}\big|_{r=0} = V_u \frac{dP_u}{dt} \text{ for } t > 0$$

Equation 3-6

$$\frac{kA}{\mu c_g} * \frac{dP}{dx}\big|_{r=L} = V_d \frac{dP_d}{dt} \text{ for } t > 0$$

Equation 3-7

where, A is cross-sectional area of the cylindrical specimen, P_u and P_d are upstream and downstream pressures, respectively, and V_u and V_d are the volumes of upstream and downstream vessels, respectively.

To solve the equations above, the specimen in finite difference form is constructed based on the point-distributed grid system (figure 3-2). The numerical scheme of governing equation 3-1 is shown below:

$$-\frac{C}{2\Delta x^2} P_{i-1}^{n+1} + \left(\frac{1}{\Delta t} + \frac{C}{\Delta x^2}\right) P_i^{n+1} - \frac{C}{2\Delta x^2} P_{i+1}^{n+1} = \left(\frac{1}{\Delta t}\right) P_i^n \text{ for } 1 \leq i \leq ng$$

Equation 3-8

where, *ng* is the number of gridblocks excluding the boundary gridblocks, *n* and *n+1* represent old and new time level, respectively, and *i* represents the center of gridblock *i*. When *i=1*, *i-1* represents the upstream location. When *i=ng*, *i+1* represents the downstream location. Δx and Δt

represent space and time step used in numerical simulation, respectively. Δx is expressed as follows:

$$\Delta x = \Delta x_1 = \Delta x_2 = \cdots = \Delta x_{ng} = \frac{L}{ng + 1}$$

<div align="right">Equation 3-9</div>

The length of the gridblock which contains left or right boundary is equal to $\frac{\Delta x}{2}$. C is expressed as:

$$C = \frac{k}{\mu c_g(\phi + (1 - \phi)K_a)}$$

<div align="right">Equation 3-10</div>

Equation 3-8 can be arranged into the matrix form to solve for the pressure distribution along the specimen at the next time step. The matrix is shown below as matrix term 3-1. However, this matrix term needs upstream and downstream pressures at the next time step as input and such pressure data can be obtained by solving the boundary conditions numerically. Equation 3-6 and equation 3-7 in numerical form is:

$$\frac{P(1)^n - P_u^n}{dx} * \frac{kA}{\mu c_g} = V_u \frac{P_u^{n+1} - P_u^n}{dt}$$

<div align="right">Equation 3-11</div>

$$\frac{P(ng)^n - P_d^n}{dx} * \frac{kA}{\mu c_g} = V_d \frac{P_d^{n+1} - P_d^n}{dt}$$

<div align="right">Equation 3-12</div>

Therefore, given the initial condition, upstream and downstream pressures at the next time step can be solved by equation 3-11 and equation 3-12. Then the pressure data can be plugged into the matrix term 3-1 to solve for pressure distribution along the specimen at the next time step. After that, pressure data of the whole system at the next time step are regarded as the initial condition

and used for the same cycle mentioned above. Flowchart 3-1 summarizes the procedure of numerical simulation.

$$
\begin{bmatrix}
\left(\dfrac{1}{\Delta t}+\dfrac{2C}{\Delta x^2}\right) & -\dfrac{C}{\Delta x^2} & 0 & 0 & \cdots & 0 & 0 & 0 \\[2mm]
-\dfrac{C}{\Delta x^2} & \left(\dfrac{1}{\Delta t}+\dfrac{2C}{\Delta x^2}\right) & -\dfrac{C}{\Delta x^2} & 0 & \cdots & 0 & 0 \\[2mm]
0 & -\dfrac{C}{\Delta x^2} & \left(\dfrac{1}{\Delta t}+\dfrac{2C}{\Delta x^2}\right) & -\dfrac{C}{\Delta x^2} & 0 & \cdots & 0 \\[2mm]
& & \vdots & & & & \\[2mm]
0 & 0 & 0 & \cdots & 0 & 0 & -\dfrac{C}{\Delta x^2} & \left(\dfrac{1}{\Delta t}+\dfrac{2C}{\Delta x^2}\right)
\end{bmatrix}
\begin{bmatrix}
P_1^{n+1} \\[1mm]
P_2^{n+1} \\[1mm]
P_3^{n+1} \\[1mm]
\vdots \\[1mm]
P_{ng}^{n+1}
\end{bmatrix}
=
\begin{bmatrix}
\dfrac{P_1^n}{\Delta t}+\dfrac{C}{\Delta x^2}P_u^{n+1} \\[2mm]
\dfrac{P_2^n}{\Delta t} \\[2mm]
\dfrac{P_3^n}{\Delta t} \\[2mm]
\vdots \\[2mm]
\dfrac{P_{ng}^n}{\Delta t}+\dfrac{C}{\Delta x^2}P_d^{n+1}
\end{bmatrix}
$$

Matrix term 3-1 Matrix term used to get the pressure distribution along the specimen
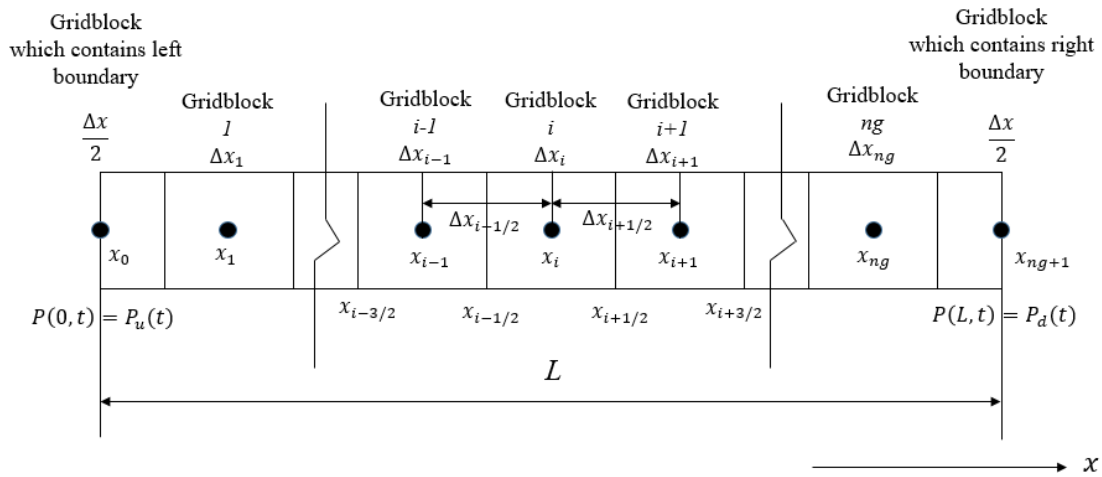
Figure 3-2 Specimen in Finite Difference Form

Initial Condition

Calculate upstream and downstream pressure at the next time step using equation 3-11 and equation 3-12

Matrix construction according to matrix term 3-1 and solving for the pressure distribution along the specimen at the next time step

Update time step, pressure distribution of the whole system and the corresponding gas properties

Final time?

End
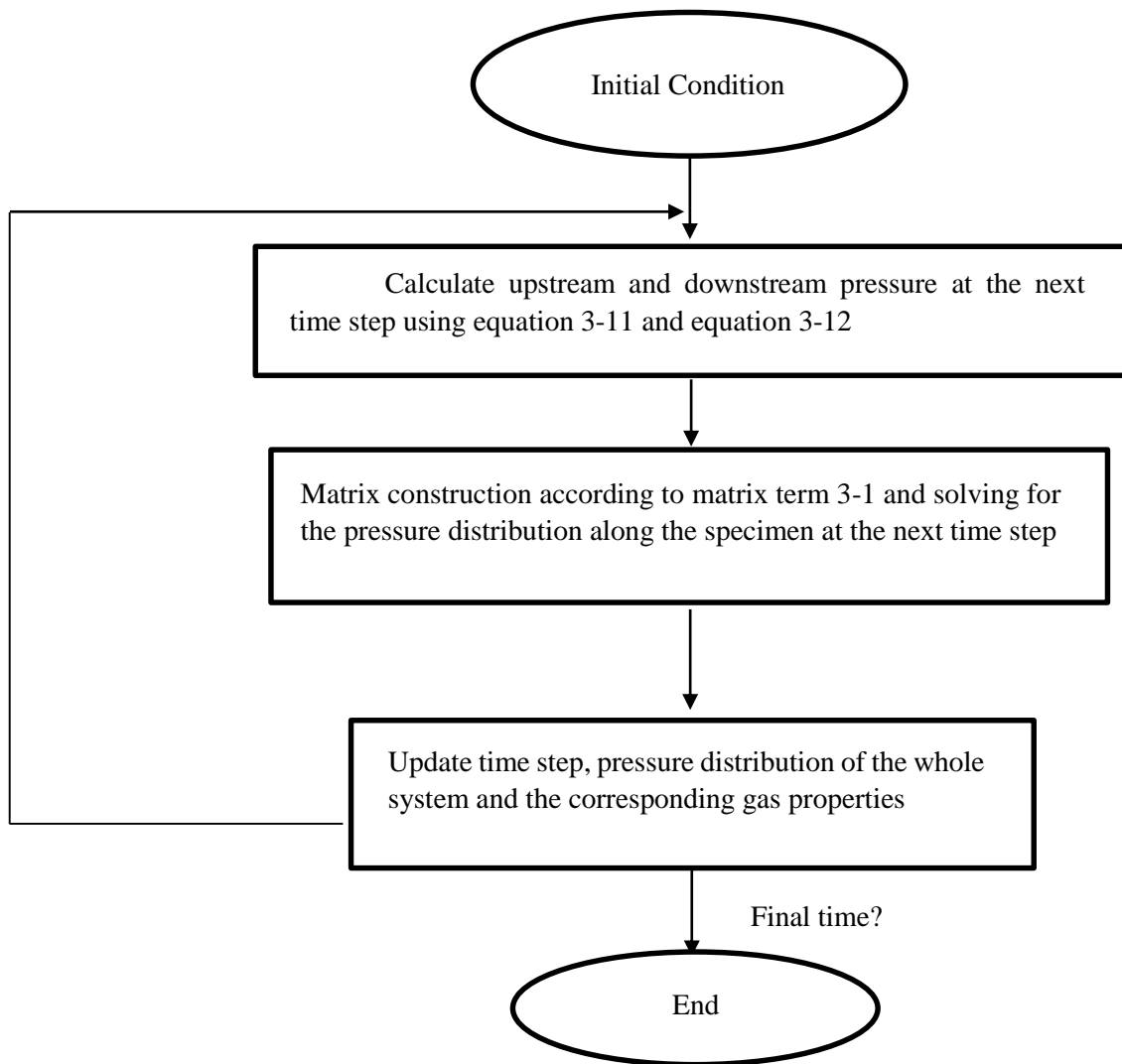
Flowchart 3-1 Procedure of numerical simulation with the assumption of constant properties

3.2.2 Numerical Simulation in This New Method

When gas properties are varied with pressure, numerical simulation is an effective tool to solve for pressure profiles. In this condition, the governing equation turns out to be (Darabi et al., 2012):

$$\phi \frac{\partial \rho}{\partial t} + (1 - \phi) \frac{\partial q}{\partial t} = \frac{\partial}{\partial x}\left(\frac{\rho k}{\mu} \frac{\partial P}{\partial x}\right) \text{ for } 0 < x < L, t > 0$$

Equation 3-13

where, q is adsorbate density per unit sample volume given as:

$$q = \frac{\rho_s q_a}{V_{std}} = \frac{\rho_s}{V_{std}} * \frac{q_L P}{P_L + P}$$

Equation 3-14

where, q_a is gas storage capacity, ρ_s is skeleton density of the sample, V_{std} is the molar volume of gas at standard pressure and temperature ($22.4*10^{-3}$m^3/mol). q_L and P_L are Langmuir volume and Langmuir pressure, respectively. The initial condition is given below:

$$P(r, 0) = P_d(0) \text{ for } 0 < r < L$$

Equation 3-15

The boundary conditions are listed as follows:

$$P(0, t) = P_u(t) \text{ for } t \geq 0$$

Equation 3-16

$$P(L, t) = P_d(t) \text{ for } t \geq 0$$

Equation 3-17

$$\frac{\rho k A}{\mu} * \frac{dP}{dx}\Big|_{r=0} = V_u \frac{d\rho_u}{dt} \text{ for } t > 0$$

Equation 3-18

$$\frac{\rho k A}{\mu} * \frac{dP}{dx}\Big|_{r=L} = V_d \frac{d\rho_d}{dt} \text{ for } t > 0$$

Equation 3-19

where, ρ_u and ρ_d are the densities corresponding to upstream and downstream pressures, respectively. The boundary equation 3-18 and equation 3-19 are based on mass balance. The gas which flows into/out of the vessel is equal to the quantity change of gas inside the vessel.

In fact, when gas properties are assumed to be constant, these equations can be reduced to the equations shown in part 3.2.1. For governing equation 3-13, it becomes:

$$\phi \frac{\partial \rho}{\partial P} * \frac{\partial P}{\partial t} + (1 - \phi) \frac{\partial q}{\partial \rho} * \frac{\partial \rho}{\partial P} * \frac{\partial P}{\partial t} = \frac{\rho k}{\mu} * \frac{\partial^2 P}{\partial x^2}$$

Equation 3-20

Since $\frac{\partial \rho}{\partial P} = \rho c_g$, equation 3-20 becomes

$$\phi \rho c_g \frac{\partial P}{\partial t} + (1 - \phi) K_a \rho c_g \frac{\partial P}{\partial t} = \frac{\rho k}{\mu} * \frac{\partial^2 P}{\partial x^2}$$

Equation 3-21

where, $K_a = \frac{\partial q}{\partial \rho} = \frac{\rho_s}{V_{std}} \frac{1}{c_g \rho} \frac{q_L P_L}{(P+P_L)^2}$. The final arrangement of the governing equation is expressed as:

$$\frac{\partial P}{\partial t} = \frac{k}{\mu c_g (\phi + (1 - \phi) K_a)} * \frac{\partial^2 P}{\partial x^2}$$

Equation 3-22

The boundary conditions shown in equation 3-18 and equation 3-19 become:

$$\frac{\rho k A}{\mu} * \frac{dP}{dx} \big|_{r=0} = V_u \frac{dP_u}{dt} \rho c_g$$

Equation 3-23

$$\frac{\rho k A}{\mu} * \frac{dP}{dx} \big|_{r=L} = V_d \frac{dP_d}{dt} \rho c_g$$

Equation 3-24

$$\frac{k A}{\mu c_g} * \frac{dP}{dx} \big|_{r=0} = V_u \frac{dP_u}{dt}$$

Equation 3-25

$$\frac{kA}{\mu c_g} * \frac{dP}{dx}\Big|_{r=L} = V_d \frac{dP_d}{dt}$$

<div align="right">Equation 3-26</div>

As a result, the governing equation and boundary equations are consistent with the equations shown in the previous part. Therefore, the only difference between these two groups of equations is constant gas properties or varied gas properties. This is beneficial because by making use of this difference, the effect of pressure-dependent gas properties on the permeability results can be investigated.

The following numerical scheme is constructed to numerically solve the governing equation 3-13:

$$\frac{\phi}{RT}\frac{(\frac{P_i^{(v+1)}}{Z_i^{(v)}})^{n+1} - (\frac{P}{Z})_i^n}{\Delta t} + (1-\phi)\frac{q_i^{(v)}{}^{n+1} - q_i{}^n}{\Delta t}$$

$$= \left(\frac{\rho k}{\mu \Delta x^2}\right)_{i+1/2}^{(v)}{}^{n+1} * P_{i+1}^{(v+1)}{}^{n+1} - \left(\left(\frac{\rho k}{\mu \Delta x^2}\right)_{i+\frac{1}{2}}^{(v)}{}^{n+1} + \left(\frac{\rho k}{\mu \Delta x^2}\right)_{i-\frac{1}{2}}^{(v)}{}^{n+1}\right) * P_i^{(v+1)}{}^{n+1} + \left(\frac{\rho k}{\mu \Delta x^2}\right)_{i-\frac{1}{2}}^{(v)}{}^{n+1} * P_{i-1}^{(v+1)}{}^{n+1} \quad \text{for } 1$$

$$\leq i \leq ng$$

<div align="right">Equation 3-27</div>

where, v represents the iteration step. The point-distributed grid system shown in figure 3-2 is still applied in this case. The terms $\left(\frac{\rho k}{\mu \Delta x^2}\right)_{i+\frac{1}{2}}$ and $\left(\frac{\rho k}{\mu \Delta x^2}\right)_{i-\frac{1}{2}}$ can be estimated by the harmonic average:

$$\frac{1}{\left(\frac{\rho k}{\mu \Delta x^2}\right)_{i+\frac{1}{2}}} = \frac{1}{2}\left[\frac{1}{\left(\frac{\rho k}{\mu \Delta x^2}\right)_i} + \frac{1}{\left(\frac{\rho k}{\mu \Delta x^2}\right)_{i+1}}\right]$$

<div align="right">Equation 3-28</div>

$$\frac{1}{\left(\frac{\rho k}{\mu \Delta x^2}\right)_{i-\frac{1}{2}}} = \frac{1}{2}\left[\frac{1}{\left(\frac{\rho k}{\mu \Delta x^2}\right)_i} + \frac{1}{\left(\frac{\rho k}{\mu \Delta x^2}\right)_{i-1}}\right]$$

<div align="right">Equation 3-29</div>

Equation 3-27 can also be arranged into the matrix form, which is shown as matrix term 3-2. The boundary equations in finite difference form are shown below:

$$\frac{P(1)^n - P_u^n}{\Delta x} * \frac{\rho k A}{\mu}\bigg|_{r=0} = V_u \frac{\rho_u^{n+1} - \rho_u^n}{\Delta t}$$

<div align="right">Equation 3-30</div>

$$\frac{P(ng)^n - P_d^n}{\Delta x} * \frac{\rho k A}{\mu}\bigg|_{r=L} = V_d \frac{\rho_d^{n+1} - \rho_d^n}{\Delta t}$$

<div align="right">Equation 3-31</div>

With initial condition given, equation 3-30 and equation 3-31 is capable of solving for upstream and downstream densities at the next time step. Iteration is needed to convert density to pressure. Flowchart 3-2 shows the procedure graphically. After that, pressure data is plugged into matrix term 3-2 to solve for pressure distribution along the specimen at the next iteration step and the solution is not found until it coverages. During this process, pressure-dependent properties (i.e. compressibility factor Z, viscosity μ, adsorbate density q and gas density ρ) are taken as a function of pressure at the previous iteration step. Varied viscosity can be obtained by NIST Standard Reference Database software. Flowchart 3-3 shows the procedure of numerical simulation. Compared with the procedure shown in part 3.2.1, the greatest advantage of numerical simulation with constant properties assumed is that it saves a lot of computation time because iteration is avoided.

$$
\begin{bmatrix}
-\left(\left(\dfrac{\phi}{RT\Delta tZ}\right)_1^{n+1} + \left(\dfrac{\rho k}{\mu\Delta x^2}\right)_{1+1/2}^{\overset{(v)}{n+1}} + \left(\dfrac{\rho k}{\mu\Delta x^2}\right)_{1-1/2}^{\overset{(v)}{n+1}}\right) & \left(\dfrac{\rho k}{\mu\Delta x^2}\right)_{1+1/2}^{\overset{(v)}{n+1}} & 0 & 0 & \cdots & 0 & 0 \\[2em]
\left(\dfrac{\rho k}{\mu\Delta x^2}\right)_{2-1/2}^{\overset{(v)}{n+1}} & -\left(\left(\dfrac{\phi}{RT\Delta tZ}\right)_2^{n+1} + \left(\dfrac{\rho k}{\mu\Delta x^2}\right)_{2+1/2}^{\overset{(v)}{n+1}} + \left(\dfrac{\rho k}{\mu\Delta x^2}\right)_{2-1/2}^{\overset{(v)}{n+1}}\right) & \left(\dfrac{\rho k}{\mu\Delta x^2}\right)_{2+1/2}^{\overset{(v)}{n+1}} & 0 & \cdots & 0 & 0 \\[2em]
0 & \left(\dfrac{\rho k}{\mu\Delta x^2}\right)_{3-1/2}^{\overset{(v)}{n+1}} & -\left(\left(\dfrac{\phi}{RT\Delta tZ}\right)_3^{n+1} + \left(\dfrac{\rho k}{\mu\Delta x^2}\right)_{3+1/2}^{\overset{(v)}{n+1}} + \left(\dfrac{\rho k}{\mu\Delta x^2}\right)_{3-1/2}^{\overset{(v)}{n+1}}\right) & \left(\dfrac{\rho k}{\mu\Delta x^2}\right)_{3+1/2}^{\overset{(v)}{n+1}} & 0 & \cdots & 0 & 0 \\[1em]
& & \vdots & & & & \\[1em]
0 & 0 & 0 & 0 \quad \cdots \quad \left(\dfrac{\rho k}{\mu\Delta x^2}\right)_{ng-1/2}^{\overset{(v)}{n+1}} & -\left(\left(\dfrac{\phi}{RT\Delta tZ}\right)_{ng}^{\overset{(v)}{n+1}} + \left(\dfrac{\rho k}{\mu\Delta x^2}\right)_{ng+1/2}^{\overset{(v)}{n+1}} + \left(\dfrac{\rho k}{\mu\Delta x^2}\right)_{ng-1/2}^{\overset{(v)}{n+1}}\right) & &
\end{bmatrix}
\begin{bmatrix}
P_1^{n+1 \,(v+1)} \\
P_2^{n+1 \,(v+1)} \\
P_3^{n+1 \,(v+1)} \\
\vdots \\
P_{ng}^{n+1 \,(v+1)}
\end{bmatrix}
$$

$$
=
\begin{bmatrix}
-\dfrac{\phi}{RT\Delta t} * \left(\dfrac{P}{Z}\right)_1^n + (1-\phi)\dfrac{q_1^{n+1} - q_1^n}{\Delta t} - \left(\dfrac{\rho k}{\mu\Delta x^2}\right)_{1-1/2}^{\overset{(v)}{n+1}} * P_u^{n+1} \\[1.5em]
-\dfrac{\phi}{RT\Delta t} * \left(\dfrac{P}{Z}\right)_2^n + (1-\phi)\dfrac{q_2^{n+1} - q_2^n}{\Delta t} \\[1.5em]
-\dfrac{\phi}{RT\Delta t} * \left(\dfrac{P}{Z}\right)_3^n + (1-\phi)\dfrac{q_3^{n+1} - q_3^n}{\Delta t} \\[1em]
\vdots \\[1em]
-\dfrac{\phi}{RT\Delta t} * \left(\dfrac{P}{Z}\right)_{ng}^n + (1-\phi)\dfrac{q_{ng}^{n+1} - q_{ng}^n}{\Delta t} - \left(\dfrac{\rho k}{\mu\Delta x^2}\right)_{ng+1/2}^{\overset{(v)}{n+1}} * P_d^{n+1}
\end{bmatrix}
$$

Matrix term 3-2 Matrix for solving governing equation

Start

Assuming an initial value of Z

Calculate molar density at the next time step using equation 3-30 and equation 3-31

Calculate the corresponding pressure using equation 3-2

Update compressibility factor as $Z1$ with the updated pressure and given temperature

$|Z-Z1|<$Tolerance?

No

$Z=Z1$

Output pressure and the compressibility factor Z
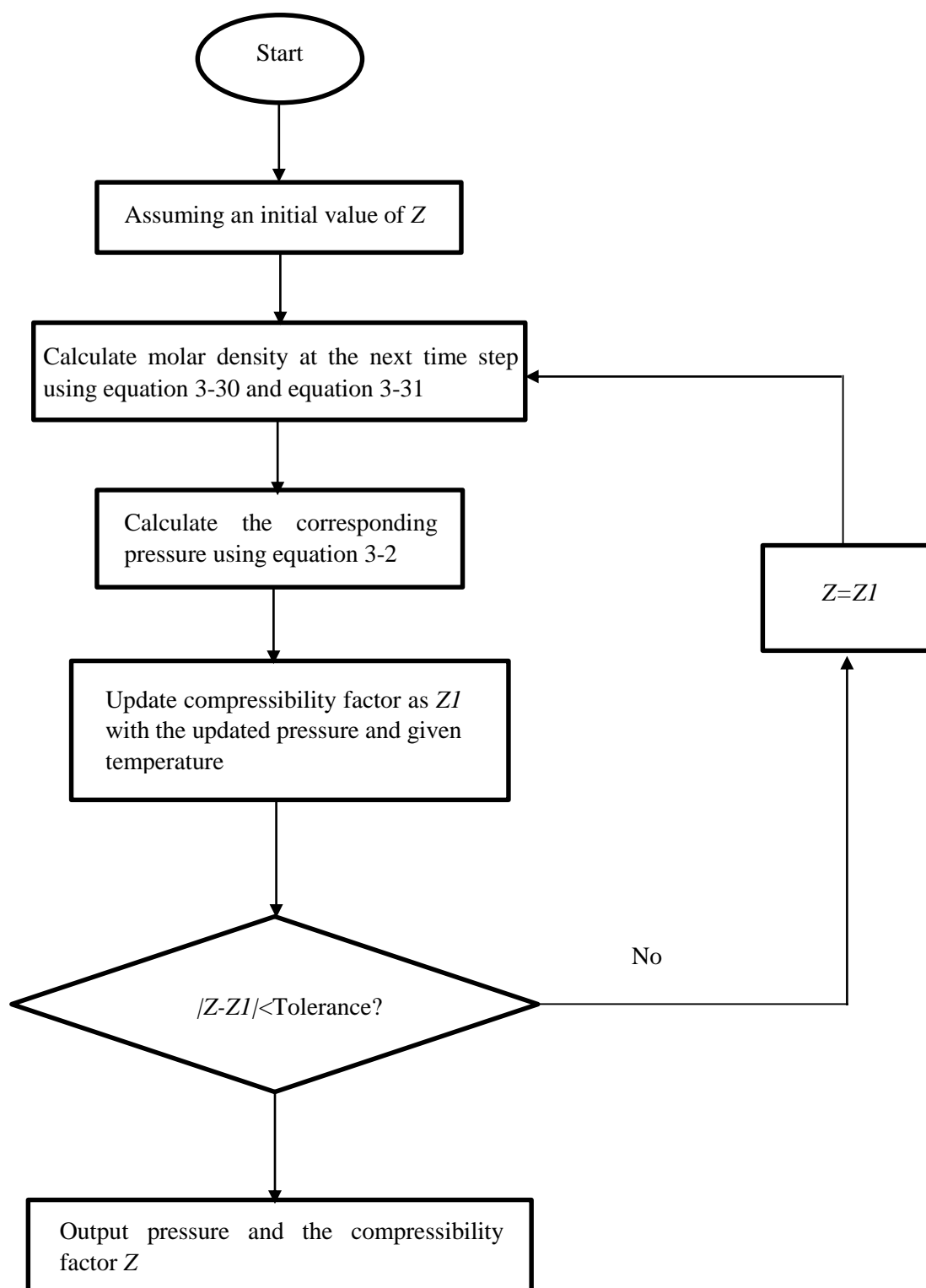
Flowchart 3-2 Procedure to convert density to pressure

Initial Condition

Calculate upstream and downstream pressure at the next time step following flowchart 3-2

Assuming an initial guess of pressure distribution along the specimen *P*. For convenience, it is equal to the pressure distribution at the previous time step

Matrix construction according to matrix term 3-2 and solving for the pressure distribution along the specimen at the next iteration step P2

P=P2

max|*P2-P*|<tolerance?

Update time step, pressure distribution of the whole system and the corresponding gas properties

End

Flowchart 3-3 Procedure of numerical simulation

3.3 Pressure History-Matching Method

Figure 3-3 shows an example of numerical simulation results under different permeabilities. It can be observed that low permeability slows down the pressure change rate while high permeability speeds up the rate of pressure convergence. This observation applies to both constant and pressure-dependent gas properties used in numerical simulation. According to Chen (2015), low permeability hinders convective transport of free gas, which results in accumulated gas molecules and higher pressure. Conversely, high permeability is favorable for gas transport leading to gas depletion and a higher pressure decline. Therefore, the shape of the pressure profile changes with permeability, and the estimated permeability should give the close fit between simulated and experimental pressure results, which can be assessed using the history-matching method. To quantify their difference, the following objective function is defined:

$$R = \frac{\left(\left(\sum_{i=1}^{N} \left(\left\| \frac{P_{ki} - P_{k1i}}{P_{k1i}} \right\| \right) \right)_{upstream} + \sum_{j=1}^{M} \left(\left\| \frac{P_{kj} - P_{k1j}}{P_{k1j}} \right\| \right)_{downstream} \right)}{N + M} * 100\%$$

Equation 3-32

where, i and j represent discrete time steps. N and M are the number of data points. P_k and P_{k1} are simulation data and experimental data, respectively. Based on a great amount of simulation work conducted, the objective function is expected to show the following behavior (figure 3-4). As permeability increases, the objective function decreases at first and then increases. To optimize the matching extent, permeability estimated should correspond to the minimum value of the objective function R. Therefore, in this study a set of permeability values are tested, and the permeability is not obtained until the minimum objective function is reached. If the minimum objective function is within the tolerance, the corresponding permeability will be applicable. In this study, the tolerance is empirically equal to 2.5%.
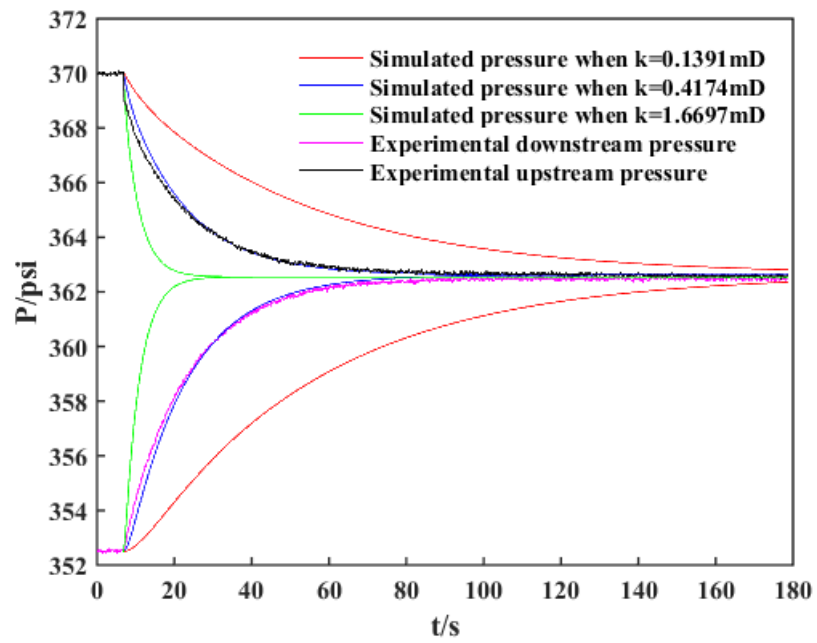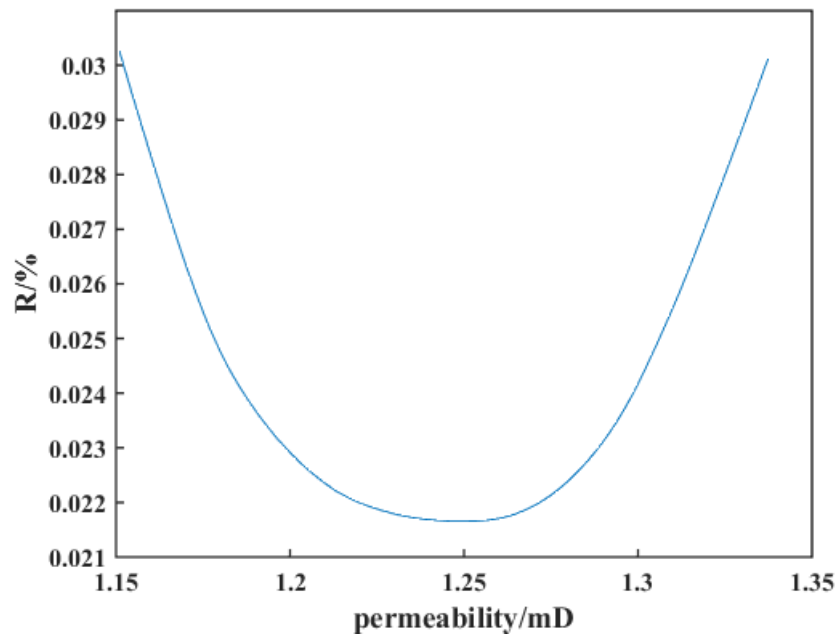
Figure 3-3 Example of History Matching

Figure 3-4 Behavior of Objective Function

Chapter 4

Result and Discussion

In this study, three types of gases including helium, methane and carbon dioxide were used to test the permeability of the sample to different gases. The first part shows the permeability results obtained by this new method. Compared with the analytical solution of Cui et al. (2009), improved permeability results are presented and such improvement can be attributed to two aspects of methodology differences. Sensitivity analysis which is detailed in section 4.2 is performed to investigate the influence of each aspect on the improvement of permeability results.

4.1 Permeability Results

4.1.1 Helium Injection

Table 4-1 shows the data input used in the permeability determination for helium. P_e corresponds to the final equilibrium pressure at each pressure step and represents the corresponding pressure for the estimated permeability. The values of viscosity μ and compressibility c_g at final equilibrium pressure P_e are shown in table 4-1, as obtained from NIST Standard Reference Database software. These constant values can be used in the analytical solution of permeability and numerical solution of permeability with the assumption of constant gas properties. The concepts of P_e and constant viscosity and compressibility also apply to the cases of methane and carbon dioxide. Porosity is empirically assumed to be 0.12.

Table 4-1 Parameter Input for Helium

	Step					
Variable	1	2	3	4	5	6
$P_{ui}(psi)$	31.33	148.13	264.25	380.33	496.43	613.38
$P_{di}(psi)$	14.71	130.48	246.72	363.15	478.51	595.35
μ $(Pa*s)$	1.9757E-05	1.9786E-05	1.9814E-05	1.9843E-05	1.9871E-05	1.9899E-05
$c_g(psi^{-1})$	0.0408	0.00708	0.00386	0.00265	0.00201	0.00162
$V_u(m^3)$	2.998E-05	2.998E-05	2.998E-05	2.998E-05	2.998E-05	2.998E-05
$V_d(m^3)$	1.78E-05	1.78E-05	1.78E-05	1.78E-05	1.78E-05	1.78E-05
$L(m)$	0.0602	0.0602	0.0602	0.0602	0.0602	0.0602
$A(m^2)$	5.07E-04	5.07E-04	5.07E-04	5.07E-04	5.07E-04	5.07E-04
ϕ	0.12	0.12	0.12	0.12	0.12	0.12
P_e (psi)	24.51	140.54	256.75	372.89	488.69	605.47

History-matching results are shown in figure 4-1. It can be observed that at each pressure step, the simulated curve is able to successfully replicate the experimental pressure profile. This can be confirmed by table 4-2, which shows that the objective function R is always within the tolerance. The permeability results are also shown in table 4-2. It can be seen that from an overall point of view, permeability increases as pressure increases from 24.5 psi to 605.5 psi. Since helium has no sorption effect, this trend can be purely attributed to decreasing effective stress: as pore pressure increases, the effective stress defined as the difference between constant confining stress and pore pressure decreases, resulting in the opening of microfracures and therefore increasing permeability (Kumar et al., 2016).

Table 4-2 Permeability Results for Helium

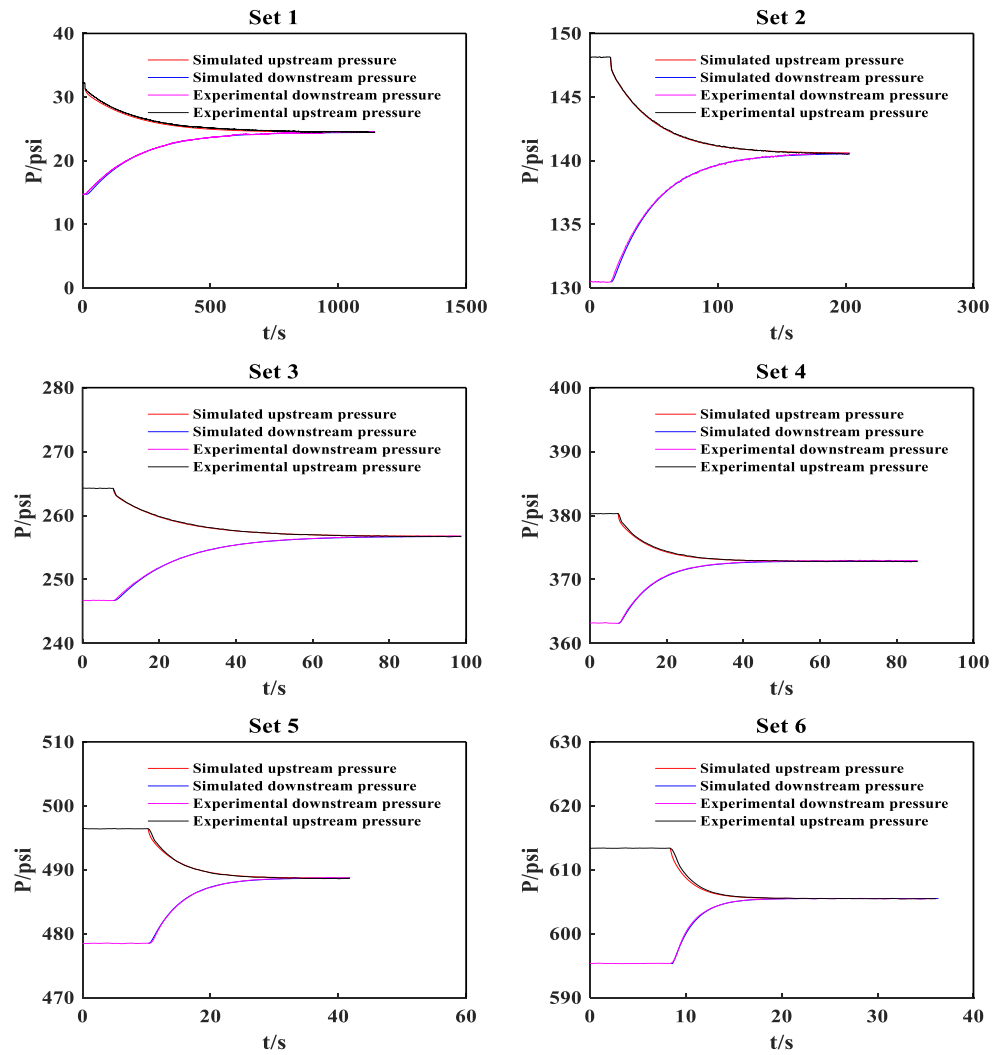| Step	Pressure(psi)	Permeability (mD)	Objective function R (%)
1	24.51	0.87	0.48
2	140.54	0.82	0.037
3	256.75	0.98	0.02
4	372.89	1.24	0.022
5	488.69	1.65	0.014
6	605.47	2.91	0.011

Figure 4-1 History-matching Result for Helium

4.1.2 Methane Injection

Table 4-3 shows the data input used in the numerical simulation for methane. Since methane is primarily stored in coal through adsorption onto the coal surface (Moore, 2012), adsorbate density q in governing equation 3-13 cannot be ignored. Therefore, based on the

Langmuir sorption modeling, the values of Langmuir pressure and Langmuir volume are needed

and must be acquired by performing another independent experiment.

Table 4-3 Parameter Input for Methane

Variable	Step					
	1	2	3	4	5	6
$P_{ui}(psi)$	32.05	141.79	256.51	370.05	482.65	610.04
$P_{di}(psi)$	14.71	124.29	238.92	352.54	464.96	592.59
$\mu\ (Pa*s)$	1.1019E-05	1.1126E-05	1.1252E-05	1.1393E-05	1.1549E-05	1.1747E-05
$c_g(psi^{-1})$	0.0424	0.00759	0.00415	0.00288	0.00223	0.00178
$V_u(m^3)$	2.998E-05	2.998E-05	2.998E-05	2.998E-05	2.998E-05	2.998E-05
$V_d(m^3)$	1.78E-05	1.78E-05	1.78E-05	1.78E-05	1.78E-05	1.78E-05
$L(m)$	0.0602	0.0602	0.0602	0.0602	0.0602	0.0602
$A(m^2)$	5.07E-04	5.07E-04	5.07E-04	5.07E-04	5.07E-04	5.07E-04
ϕ	0.12	0.12	0.12	0.12	0.12	0.12
$P_e\ (psi)$	23.64	133.87	248.59	362.58	474.98	602.45
$qL(scf/ton)$	393.3	393.3	393.3	393.3	393.3	393.3
$pL(psi)$	380.24	380.24	380.24	380.24	380.24	380.24

History-matching results are shown in figure 4-2. The experimental pressure profile shows

that the system pressure declines after initial stabilization between upstream and downstream

pressure. This can be attributed to the sorption effect and results in enhanced storage capacity of

the sample (Aljamaan et al., 2013). Because the pressure history data after initial stabilization does

not apply to the governing equation 3-13, the pressure profile excluding the system pressure decline

is used for permeability determination. P_e refers to the initial stabilized pressure.

Table 4-4 shows the values of permeability and the objective function R. It can be observed

that permeability increases from 0.25 to 0.87 mD with pressure increasing from 23.6 psi to 602.4

psi. This trend can be attributed to the following mechanisms: methane permeability in coal is

controlled by effective stress and sorption-induced matrix swelling/shrinkage (Shi and Durucan,

2005; Liu and Harpalani, 2013a). As pore pressure increases, methane keeps adsorbing onto the

coal surface, which results in the swelling of the matrix and reduction in permeability (Pan and

Connell, 2007; Liu and Harpalani, 2013a). Simultaneously, effective stress decreases tending to open the fracture and enhance the permeability (Mazumder and Wolf, 2008; Palmer and Mansoori, 1998). Due to the fact that the permeability keeps increasing with pressure, it can be concluded that for methane permeability, decreasing effective stress is the primary factor that affects permeability change. Although sorption-induced matrix swelling exists, it is not the dominant effect during this injection process.

Table 4-4 Permeability Results for Methane

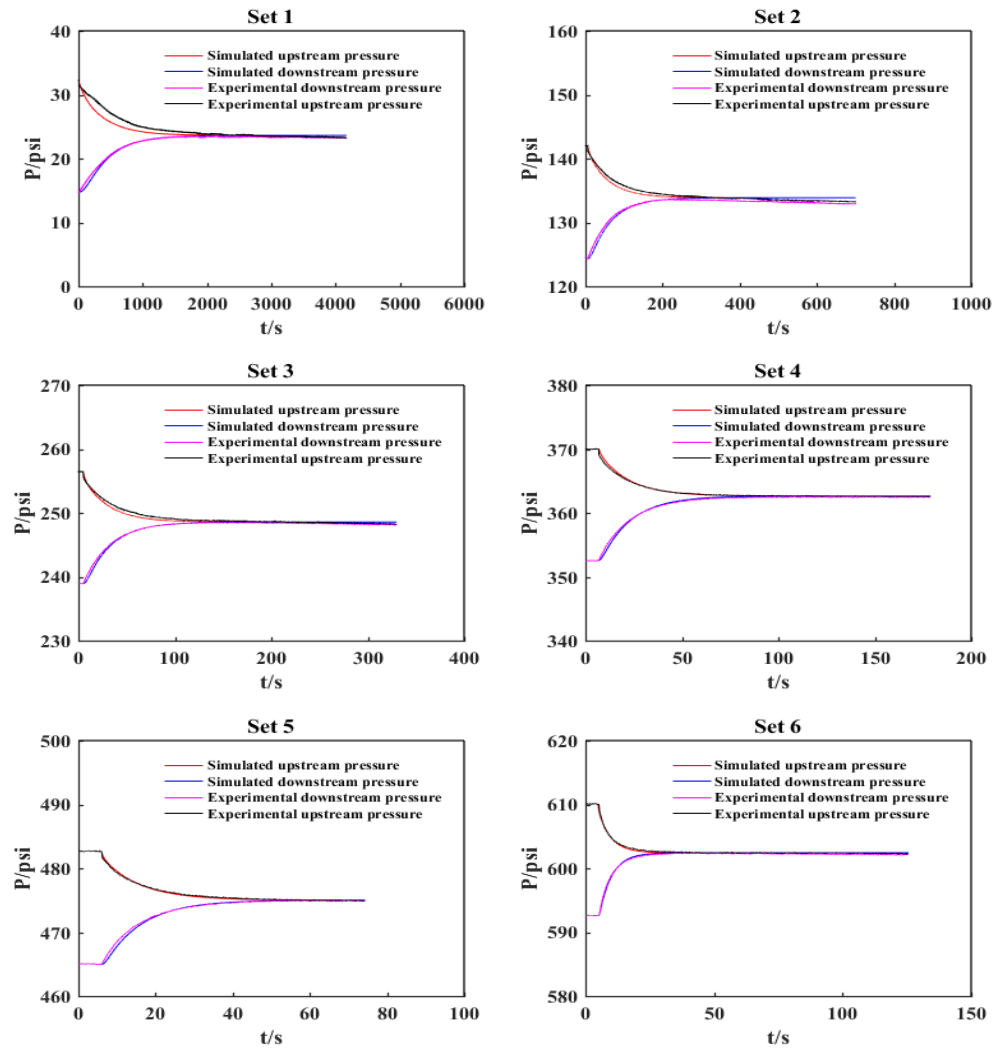| Step	Pressure (psi)	Permeability (mD)	Objective function R (%)
1	23.64	0.25	1.90
2	133.87	0.31	0.26
3	248.59	0.36	0.098
4	362.58	0.42	0.03
5	474.98	0.54	0.026
6	602.41	0.87	0.022

Figure 4-2 History-matching Result for Methane

4.1.3 Carbon Dioxide Injection

Table 4-5 shows the data input used in the numerical simulation for carbon dioxide. Carbon dioxide is an extremely adsorptive gas compared with CH_4 and He (Zoback et al., 2013), which can be confirmed by evaluating the Langmuir volume and Langmuir pressure of these different types

of gases. According to equation 3-14, at the same pressure, the amount of carbon dioxide adsorbed is larger than either methane or helium given its larger Langmuir volume and smaller Langmuir pressure. In addition, the experimental pressure profiles (figure 4-3) show larger pressure declines than helium or methane after initial pressure stabilization, which demonstrates the strong sorption effect of CO_2.

Table 4-5 Parameter Input for Carbon Dioxide

Variable	Step					
	1	2	3	4	5	6
$P_{ui}(psi)$	32.20	118.64	231.85	348.23	476.88	592.30
$P_{di}(psi)$	14.70	101.15	214.85	330.48	459.31	574.93
$\mu\ (Pa*s)$	1.4839E-05	1.4898E-05	1.5014E-05	1.5190E-05	1.5482E-05	1.5879E-05
$c_g(psi^{-1})$	0.0460	0.00955	0.00491	0.00344	0.00273	0.00245
$V_u(m^3)$	2.998E-05	2.998E-05	2.998E-05	2.998E-05	2.998E-05	2.998E-05
$V_d(m^3)$	1.78E-05	1.78E-05	1.78E-05	1.78E-05	1.78E-05	1.78E-05
$L(m)$	0.0602	0.0602	0.0602	0.0602	0.0602	0.0602
$A(m^2)$	5.07E-04	5.07E-04	5.07E-04	5.07E-04	5.07E-04	5.07E-04
ϕ	0.12	0.12	0.12	0.12	0.12	0.12
$P_e(psi)$	21.90	109.12	223.35	339.52	468.46	584.19
$qL(scf/ton)$	1170	1170	1170	1170	1170	1170
$pL(psi)$	287.41	287.41	287.41	287.41	287.41	287.41

History-matching results are shown in figure 4-3 and the corresponding permeability results are listed in table 4-6. The permeability results show that as pressure increases, permeability initially decreases and then starts to recover. This can be explained by the combined effects of sorption-induced swelling and effective stress. Compared with methane, although the factors controlling permeability are the same, the influence of each factor is different. At first the dominant effect is a significant amount of CO_2 adsorbed, inducing the swelling of the matrix. Therefore, the flow channel is narrowed down and permeability decreases. When pore pressure continues to increase, because of the characteristics of Langmuir-type sorption effect, the amount of CO_2 adsorbed increases less so that there is less influence of swelling-induced permeability reduction.

As a result, decreasing effective stress overcomes the opposite effect of swelling strain associated with gas adsorption and permeability increases through sorption-induced matrix swelling.

This permeability behavior is consistent with previous measurements conducted by Wang et al., (2011) and Li et al. (2013). One important finding that needs to be noticed is that permeability does not recover to or exceed its original value. This phenomenon is similar to that reported by Wang et al. (2015). In his research work, the depletion process in contrast to gas injection is applied; the result shows that, with pressure depletion, permeability initially decreases and then increases, but it cannot recover to its original value. According to his investigation, the reason for this is probably because the structure of anthracite is tight, and sorption-induced matrix shrinkage for anthracite is comparatively less than bituminous coals. Similarly, in this study the reasons why permeability cannot recover should include the following: (1) according to table 4-6, initial permeability is typically high. (2) Because of the significant sorption effect and tight structure of Illinois coal, decreasing effective stress cannot completely compensate for sorption-induced permeability loss.

Table 4-6 Permeability Results for Carbon Dioxide

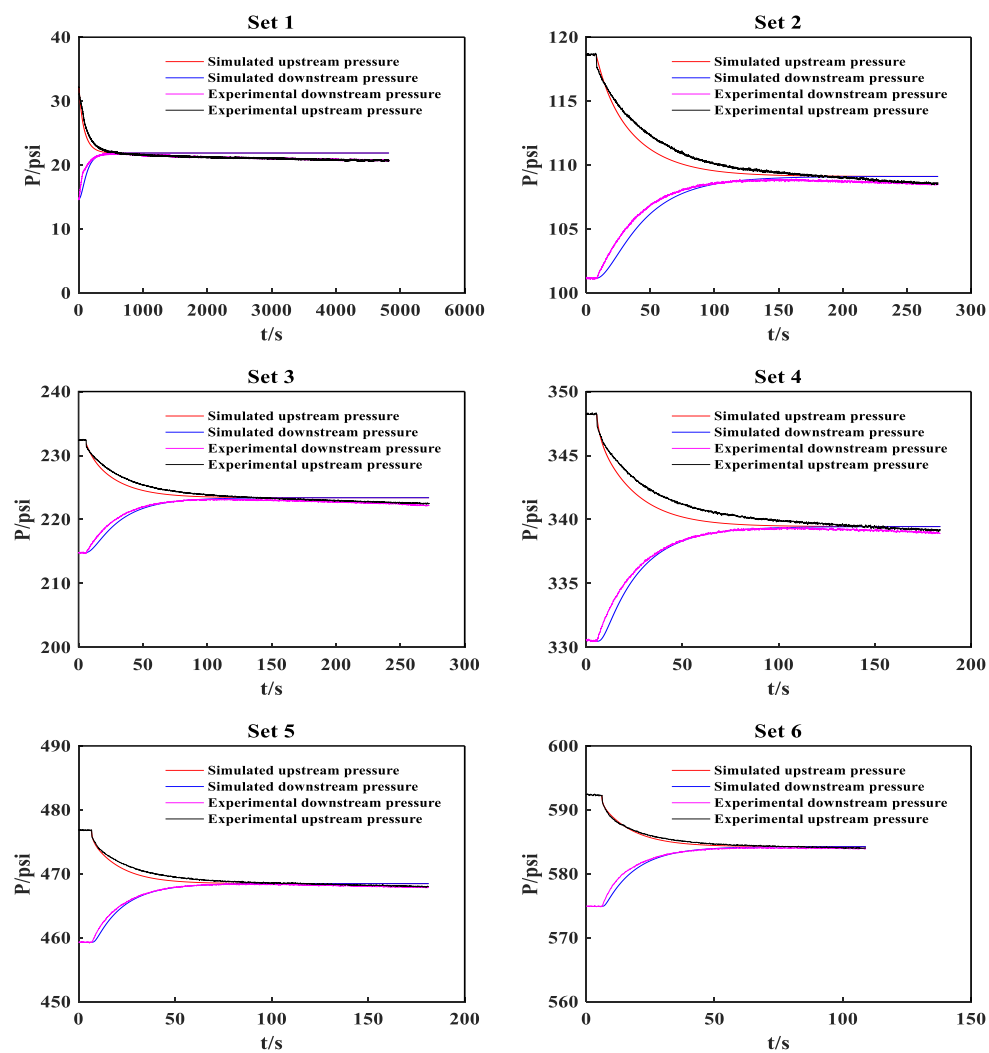| Step	Pressure(psi)	Permeability (mD)	Objective function R (%)
1	21.9	1.48	2.40
2	109.12	0.90	0.38
3	223.35	0.62	0.21
4	339.52	0.55	0.12
5	468.46	0.59	0.069
6	584.19	0.66	0.045

Figure 4-3 History-matching Result for Carbon Dioxide

4.1.4 Permeability Comparison among Different Types of Gases

      In this section, helium, methane and carbon dioxide permeabilities are used for comparison. Figure 4-4 shows the result graphically. It illustrates that helium permeability is highest when pore pressure is over 150 psi. Several reasons can be used to explain this: (1) helium is a type of non-sorbing gas so that the effect of sorption-induced matrix swelling doesn't exist. For methane and carbon dioxide, the amount of gas adsorbed is larger at higher pressure based on Langmuir modeling. (2) the molecular diameter of helium is 0.26nm, which is smallest among these three types of gas (methane: 0.38nm; carbon dioxide: 0.33nm), therefore, the transport of helium can additionally access smaller pores while methane and carbon dioxide can only flow in larger pores. (3) According to the equation of slip factor shown in equation 4-1 (Wang et al., 2015):

$$b_{CO_2} = \frac{\mu_{CO_2}}{\mu_{He}} * \sqrt{\frac{M_{He}}{M_{CO_2}}} * b_{He}$$

Equation 4-1

where, b_{CO_2} is the slip factor for carbon dioxide and b_{He} is the slip factor for helium; μ_{CO_2} and μ_{He} are the kinetic viscosity for carbon dioxide and helium, respectively; M_{CO_2} and M_{He} are the molecular weights for carbon dioxide and helium, respectively. In this study the viscosity of CO_2 is always smaller than helium viscosity based on NIST data, while molecular weight for CO_2 is always higher than helium. Therefore, the slip factor for helium is always higher than carbon dioxide so that the Klinkenberg effect on helium is more apparent than carbon dioxide.

      By comparing the permeability results of two different types of adsorptive gases (methane and carbon dioxide), it can be observed that when the pore pressure is less than 300 psi, CO_2 permeability keeps decreasing while the methane permeability keeps increasing, which indicates the extreme adsorptive characteristics of CO_2 to overcome the permeability increment induced by decreasing effective stress.

Another thing that needs to be noticed is that the permeability of CO_2 is largest at low pressures (below 100 psi). This is unexpected because CO_2 is the most adsorptive gas with a large molecular diameter. According to the modeling put forward by Zoback et al. (2013), equation 4-2 may partially explain this phenomenon:

$$k_{avg} = \frac{\sum_{i=1}^{3} k_i h_i}{\sum_{i=1}^{3} h_i} \ (k_1 > k_2 > k_3)$$

Equation 4-2

where, k_i is permeability of layer i and h_i is the thickness of layer i. This model states that the sample can be divided into various layers with different permeabilities arranged in parallel. Since the molecular diameter of helium is smallest, it can access three layers. However, due to the size of CO_2, it only accesses two layers with k_1 and k_2 taken into account. Therefore, the resulting permeability for CO_2 will be larger since we take the sum of two biggest permeabilities whereas the sum over 3 layers is taken for helium. Although less sorption and more gas slippage effect is shown for helium, CO_2 permeability remains the larger one when pressure is low.
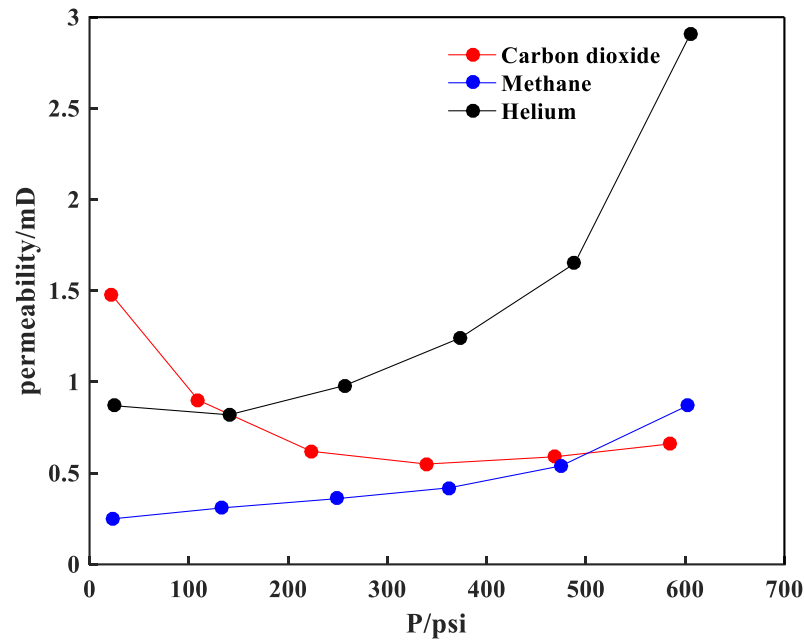
Figure 4-4 Evolution of Coal Permeability as a Function of Pore Pressure

4.2 Sensitivity Analysis

In this part, sensitivity analysis is performed to investigate the factors that influence permeability results. The differences between this new method and the analytical solution of Cui et al. (2009) are the gas properties, which are pressure-dependent or constant, and the method of permeability estimation, which refers to adopting the history-matching method or matching the late-time slope. Part 4.2.1 compares permeability results obtained by different methods to investigate the effect of methodology differences on permeability results. Part 4.2.2 investigates the influences of different inputs on the simulated differential pressure defined in equation 2-17. By varying each factor separately while keeping all other parameters fixed, the numerical procedure detailed in part 3.2.2 is used to determine the differential pressure versus time. As a result, different profiles of simulated differential pressure corresponding to different values of the assigned variable can be obtained. The factors include porosity and Langmuir pressure and Langmuir volume. The

condition of CO_2 at the 6th pressure step is used for investigation. Since the rate of differential pressure decay is related to permeability, if differential pressure curves overlap each other, permeability result will be expected to change little with the variation of the factor.

4.2.1 The Comparison of Permeability Results Obtained by Different Methods

In this part, permeability results obtained by the following three methods are used for comparison:

(1) Analytical solution. For the analytical solution, the late-time slope s_1 (after reaching 90% decay in initial differential pressure) is taken in equation 2-8 (Cronin, 2014). This is named as 'analytical solution.'

(2) Numerical solution of permeability obtained by the new method in this paper. The results are listed in part 4.1. This is named as 'numerical solution 1.'

(3) Numerical solution of permeability assuming constant parameters. The procedure of numerical simulation is introduced in part 3.2.1. After pressure profile is simulated, the history-matching method is used to get permeability. This is named as 'numerical solution 2.'

Table 4-7 Analytical Solution and Numerical Solution of Specimen Permeability to Helium

Step	Pressure(psi)	Analytical solution (mD)	Numerical solution 2 (mD)
1	24.51	0.72	0.82
2	140.54	0.84	0.82
3	256.75	1	0.97
4	372.89	1.28	1.23
5	488.69	1.8	1.62
6	605.47	3.02	2.87

Table 4-8 Analytical Solution and Numerical Solution of Specimen Permeability to Methane

Step	Pressure(psi)	Analytical solution (mD)	Numerical solution 2 (mD)
1	23.64	0.19	0.24
2	133.87	0.28	0.3
3	248.59	0.31	0.36
4	362.58	0.42	0.41
5	474.98	0.45	0.53
6	602.45	0.62	0.85

Table 4-9 Analytical Solution and Numerical Solution of Specimen Permeability to Carbon Dioxide

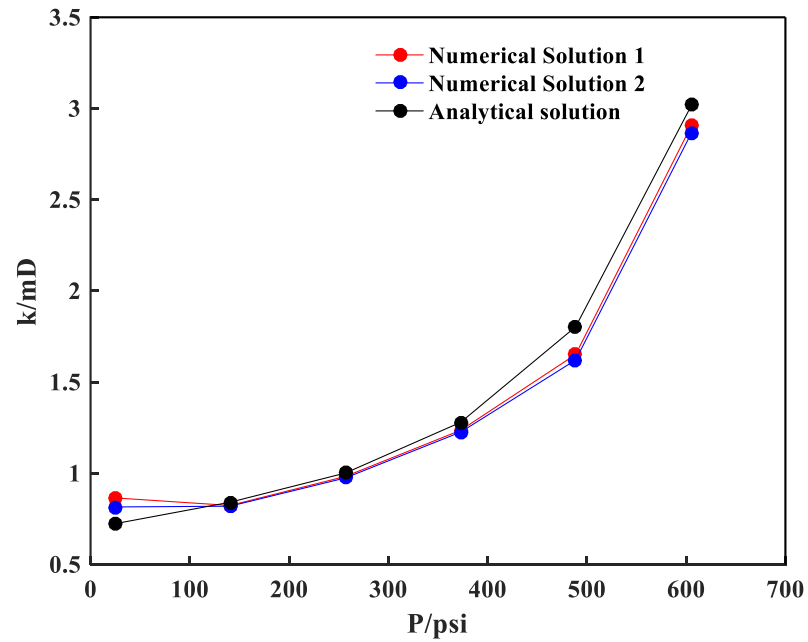| Step	Pressure(psi)	Analytical solution (mD)	Numerical solution 2 (mD)
1	21.9	1.75	1.43
2	109.12	0.88	0.89
3	223.35	0.54	0.62
4	339.52	0.38	0.55
5	468.46	0.41	0.58
6	584.19	0.47	0.66

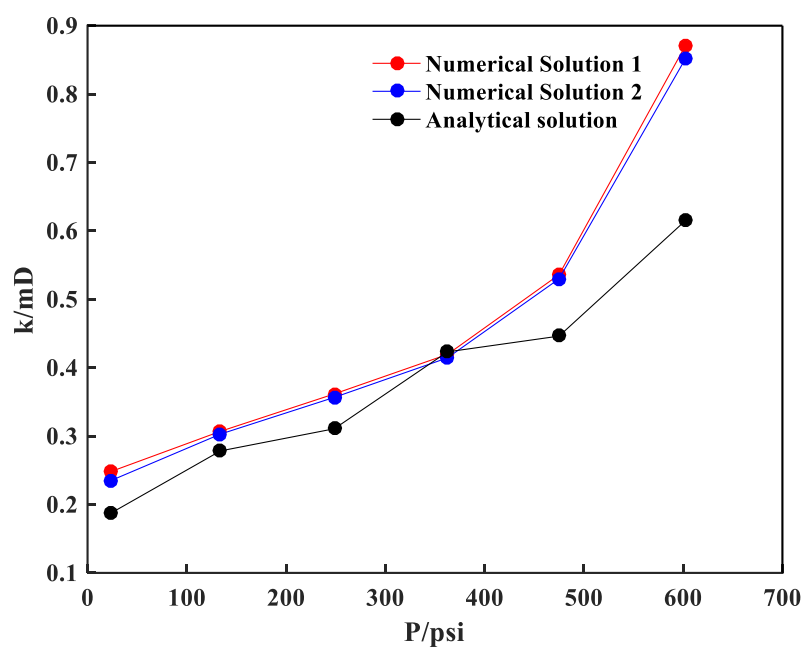Figure 4-5 Permeability Comparison for Helium

Figure 4-6 Permeability Comparison for Methane

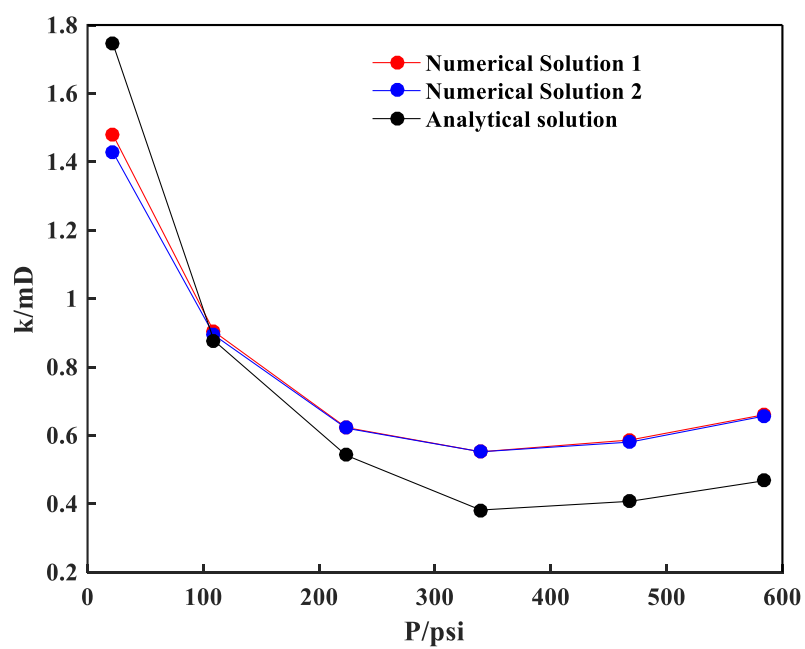Figure 4-7 Permeability Comparison for Carbon Dioxide

Table 4-10 Relative Error (%) between Different Solutions

Gas type	Solution type	Step 1 Numerical solution 2	Step 2 Numerical solution 2	Step 3 Numerical solution 2
Helium	Analytical solution	11.29	2.65	2.76
	Numerical solution 1	6.09	0.49	0.83
Methane	Analytical solution	20.24	8.12	12.86
	Numerical solution 1	5.60	1.34	1.42
Carbon Dioxide	Analytical solution	22.19	1.81	12.76
	Numerical solution 1	3.55	1.13	0.33

Table 4-11 Relative Error (%) between Different Solutions (Continued)

Gas type	Solution type	Step 1 Numerical solution 2	Step 2 Numerical solution 2	Step 3 Numerical solution 2
Helium	Analytical solution	4.39	11.25	5.28
	Numerical solution 1	0.83	1.88	1.41
Methane	Analytical solution	2.12	15.79	27.8
	Numerical solution 1	1.22	1.15	2.26
Carbon Dioxide	Analytical solution	30.84	29.83	28.79
	Numerical solution 1	0	1.05	0.62

Table 4-7-4-9 shows the analytical solution and numerical solution 2 for helium, methane and carbon dioxide, respectively. Figure 4-5-4-7 compares the permeability results graphically. It can be concluded that for each type of gas, the differences between the analytical solution of permeability and numerical solution 1 can be observed, which can be attributed to the following factors: (1) pressure-dependent gas properties or constant properties that are applied. According to Darabi et al. (2012), if the initial core pressure is low or the pressure difference across the sample is large, the analytical solution may lead to a significant error because of constant properties assumed. In this study, noting that the pressure drop at each pressure step is similar (around 17 psi), only the effect of low core pressure at initial condition can be investigated. This is achieved by comparing numerical solution 1 with numerical solution 2 because the fundamental difference between these two solutions is pressure-dependent gas properties or constant properties assumed;

(2) the analytical solution of permeability is obtained by matching the late-time slope of pressure decay, while the numerical solution of permeability is obtained by finding the best fit between simulated and experimental pressure profiles. The effect of the second factor on the permeability results can be investigated by comparing the analytical solution with numerical solution 2 because the fundamental difference between these two methods lies at the second factor. Table 4-10 and table 4-11 compare the permeability results in the form of relative error. The relative error is defined as the ratio of the difference between numerical solution 1 and numerical solution 2 or between the analytical solution and numerical solution 2 to numerical solution 2.

For the first factor, from figure 4-5-4-7 it can be observed that for each type of gas, when the initial core pressure is high, numerical solutions 1 and 2 are almost the same. The relative error data confirm this statement because they do not exceed 2% and make the assumption of constant parameters applicable. However, when the initial pressure is low (i.e. the first pressure step), the permeability difference is not consistent with the deduction of Darabi et al. (2012). Although the difference can be clearly observed, the relative error (the maximum value is 6%) cannot be regarded as a 'significant error,' especially when the relative error induced by the second factor is also calculated and used for comparison. Therefore, 17 psi can be regarded as a 'slight' pressure difference. Even when the initial core pressure is low, it does not affect permeability significantly.

Regarding the second factor, it can be observed from table 4-10 and table 4-11 that for each type of gas, at most of the pressure steps the relative error induced by the second factor is much larger than the relative error induced by using varied properties or constant properties. Only one pressure step shows comparable relative errors. Therefore, the second factor imposes larger influence on the permeability result. This phenomenon is because the experimental pressure data may not follow exactly the same trends as those for simulated curves, only matching the late-time slope does not ensure the best fit between simulated and experimental pressure profiles. For helium, such relative error reaches 10% and is usually 5-10 times the value of relative error induced by

using varied properties. However, for adsorptive gas, because of the increased complexity of flow mechanisms inside, such error can be as large as 31% and can be 10-40 times larger than another relative error.

Based on the investigation of these two factors, it can be concluded that in this study the second factor plays an important role in affecting permeability values. Therefore, the history-matching method is more reliable in permeability estimation. At the first pressure step, it is better to use pressure-dependent gas properties to improve the accuracy of permeability estimation. However, as pressure increases, considering the computation time its effect can be considered negligible, and using constant gas properties is more efficient.

4.2.2 Sensitivity of Differential Pressure to Different Factors

4.2.2.1 Porosity

The sensitivity of differential pressure to porosity is studied by considering the following values of porosity successively: 0.001, 0.01, 0.05, 0.08, 0.12, and 0.15. The rest of the parameters are specified by referring to the data from table 4-5, and a constant permeability of 0.66 mD is used. The results are shown in figure 4-8. It can be seen that simulated differential pressure curves are similar in terms of their decay characteristics. Therefore, it can be concluded that porosity variation does not significantly affect the permeability result given a certain experimental profile of differential pressure.

Notably, this conclusion seems contrary to the permeability-porosity relations that have been developed (Berg, 1970; Nelson, 1994; Pan and Connell, 2012). According to Pan and Connell (2012), permeability with respect to porosity is expected to show the following behavior based on the matchstick model:

$$\frac{k}{k_0} = (\frac{\phi}{\phi_0})^3$$

<div align="right">Equation 4-3</div>

From this equation it can be seen that when porosity reduces from 0.15 to 0.001, permeability should reduce greatly. Therefore, a proper conclusion is that specimens having different porosities tend to give different experimental results of differential pressure dP_d so that permeability varies. However, for a certain experimental curve of dP_d, noting that various porosities assumed generate comparable simulation results, the estimated permeability will change little.
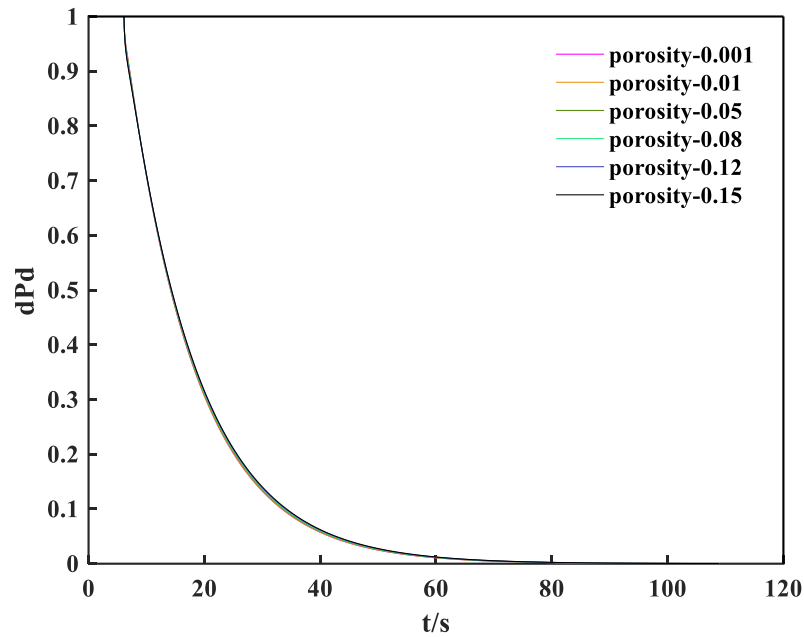

Figure 4-8 Differential Pressure under Different Porosities

4.2.2.2 Langmuir Pressure (pL) and Langmuir Volume (qL)

The effect of Langmuir pressure and Langmuir volume on the differential pressure is studied by varying each parameter separately and taking the values of other parameters from table 4-5. In this section the permeability is still equal to 0.66 mD. Langmuir pressure ranges from 100

psi to 450 psi, and Langmuir volume ranges from 800 scf/ton to 1300 scf/ton. The results are shown in figure 4-9 and figure 4-10. From the results it can be observed that the curves corresponding to different Langmuir pressures or Langmuir volumes are so close to each other that they almost merge into one curve. Therefore it can be concluded that based on a certain experimental result, permeability estimated will change slightly within a certain range of Langmuir pressures or Langmuir volumes.
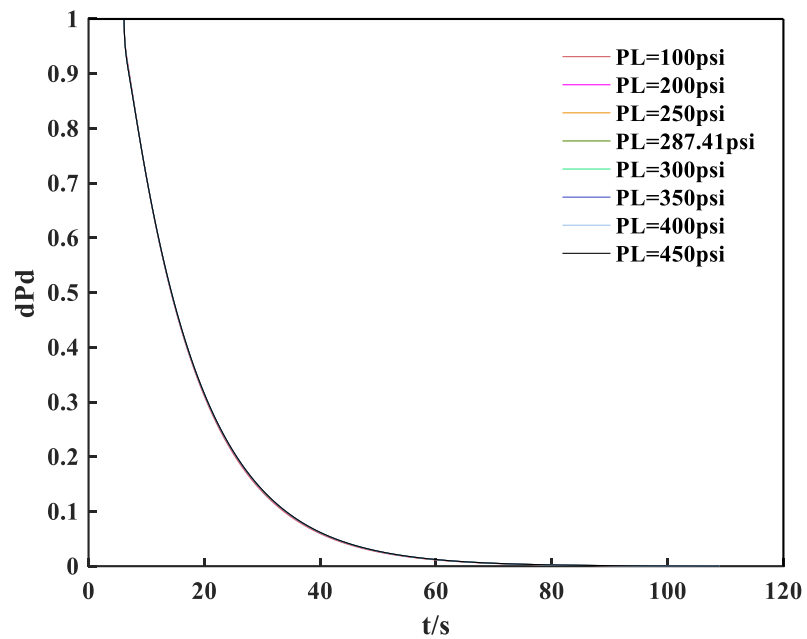

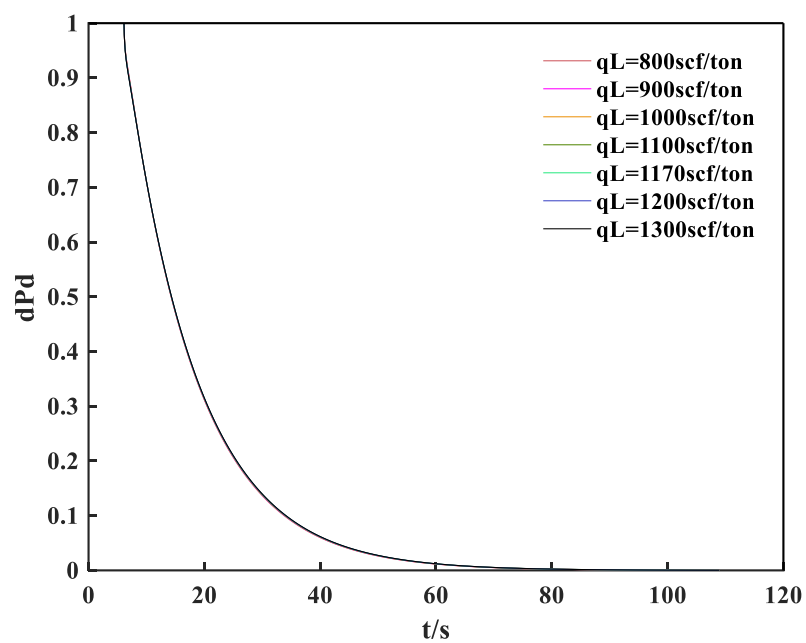Figure 4-9 Differential Pressure under Different Langmuir Pressures

Figure 4-10 Differential Pressure under Different Langmuir Volumes

Chapter 5

Conclusion

Pulse-decay experimentation is a popular method to measure the permeability of tight rock such as coal or shale. The experiment results in the pressure profile from which permeability can be inferred. In this study, a new method which combines pulse-decay experiment with numerical simulation is used to interpret permeability. Numerical simulation can be used to solve the governing equation which contains pressure-dependent gas properties and ascertain the simulated pressure profile. The desired permeability should give the best fit between simulated and experimental pressure profiles, which can be quantified by the history-matching method. This new method of permeability interpretation is tested by measuring the permeability of Illinois coal. The results show similar trends of permeability evolution with pressure, but improved permeability results compared with the analytical solutions of Cui et al. (2009). Such improvement can be attributed to the differences of methodology which fall into two aspects: (1) gas properties are assumed to be constant in the analytical solution, while in my method gas properties are pressure-dependent; (2) the analytical solution of permeability is acquired by making simulated and experimental pressure profiles have the same late-time slope. In my method, however, permeability is obtained by the history-matching method, which ensures the best fit between simulated and experimental pressure profiles. To investigate the effect of each factor on the permeability results, sensitivity analysis is conducted. Based on the work completed, the following conclusions can be made:

(1) Helium permeability increases as pressure increases. This can be attributed to decreasing effective stress. However, different permeability behaviors are exhibited by different types of sorptive gases. For methane permeability, the effect of decreasing effective stress is always greater

than sorption-induced matrix swelling so that permeability keeps increasing. For carbon dioxide, the sorption effect is dominant at first so that permeability decreases. When the effect of decreasing effective stress is strong enough, permeability starts to recover, but it cannot completely compensate for the sorption-induced permeability loss. By comparing the permeability values of these three types of gases, it can be observed that carbon dioxide permeability is largest when pressure is below 110 psi, and helium permeability is largest when the pressure is over 150 psi.

(2) For the first aspect of the methodology differences, its effect on the permeability results is not significant. When pressure is large, the relative error of permeability results induced by the first factor does not exceed 2%. Considering the computation time required for running the case of pressure-dependent properties, such error can be considered negligible. At the first pressure step (i.e. low pressures), differences between permeability results obtained under the assumption of pressure-dependent properties and constant properties are relatively apparent, and the relative error can be as high as 6%. This insignificant effect is because the initial pressure difference across the specimen for each type of gas at each pressure step (17 psi) is not large, and gas properties do not vary much within this range.

(3) The second aspect of the methodology differences imposes larger influence on permeability results. Comparison results show that for each type of gas, the relative error of permeability results induced by the second factor is many times larger than the relative error induced by the first factor at most of the pressure steps; its maximum value can be up to 31%. This is because the simulated pressure profiles may not follow exactly the same trends as those for experimental curves; therefore, only matching the late-time slope does not ensure the best fit between simulated and experimental pressure profiles. As a result, the history-matching method can be a good alternative to determine permeability.

(4) Sensitivity analysis also indicates that pressure decay characteristics change slightly with variations of porosity, Langmuir pressure, or Langmuir volume. Therefore, with a certain pulse-

decay experimental curve given, the permeability result is expected to change slightly if different values of porosity, Langmuir pressure, or volume are assumed.

References

Alharthy, N., Kobaisi, M. Al, Torcuk, M.A., Kazemi, H., Graves, R., 2012. Physics and modeling of gas flow in shale reservoirs. Abu Dhabi Int. Pet. Exhib. Conf. 4. doi:10.2118/161893-MS

Aljamaan, H., Alnoaimi, K., Kovscek, A.R., 2013. In-Depth Experimental Investigation of Shale Physical and Transport Properties. Unconv. Resour. Technol. Conf. doi:10.1190/urtec2013-114

Alnoaimi, K.R., Kovscek, A.R., 2013. Experimental and numerical analysis of gas transport in shale including the role of sorption. SPE Annu. Tech. Conf. Exhib. SPE 166375. doi:10.2118/166375-MS

Amaefule, J.O., Wolfe, K., Walls, J.D., Ajufo, A.O., Peterson, E., 1986. Laboratory determination of effective liquid permeability in low-quality reservoir rocks by the pulse decay technique. SPE Calif. Reg. Meet.

Aminian, K., 2007. Coalbed Methane- Fundamental Concepts. Pet. Nat. Gas Eng. Dep. West Virginia Univ.

Berg, R.R., 1970. Method For Determining Permeability From Reservoir Rock Properties.

Bourbie, T., Walls, J., 1982. Pulse decay permeability: analytical solution and experimental test. Soc. Pet. Eng. J. 22, 719–721. doi:10.2118/9744-PA

Brace, W.F., Walsh, J.B., Frangos, W.T., 1968. Permeability of Granite under High Pressure. J. Geophys. Res. 73, 2225–2236.

Brown, G.P., Dinardo, A., Cheng, G.K., Sherwood, T.K., 1946. The flow of gases in pipes at low pressures. J. Appl. Phys. 17, 802–813. doi:10.1063/1.1707647

Chen, C., 2015. Investigation of Gas Transport in Shale Reservoirs Using Multiscale Modeling and Principal Component Analysis. SPE Annu. Tech. Conf. Exhib.

Chen, Y., Liu, D., Yao, Y., Cai, Y., Chen, L., 2015. Dynamic permeability change during coalbed methane production and its controlling factors. J. Nat. Gas Sci. Eng. 25, 335–346. doi:10.1016/j.jngse.2015.05.018

Cronin, M.B., 2014. Core-scale heterogeneity and dual-permeability pore structure in the Barnett Shale.

Cui, X., Bustin, A.M.M., Bustin, R.M., 2009. Measurements of gas permeability and diffusivity of tight reservoir rocks: Different approaches and their applications. Geofluids 9, 208–223. doi:10.1111/j.1468-8123.2009.00244.x

Czerw, K., 2011. Methane and carbon dioxide sorption/desorption on bituminous coal-Experiments on cubicoid sample cut from the primal coal lump. Int. J. Coal Geol. 85, 72–77. doi:10.1016/j.coal.2010.10.002

Damberger, H.H., Demir, I., 1999. Coalbed and coal mine methane in the Illinois basin: Occurrence, composition and origin, and current activities. Abstr. Pap. Am. Chem. Soc. 217.

Darabi, H., Ettehad, A., Javadpour, F., Sepehrnoori, K., 2012. Gas flow in ultra-tight shale strata. J. Fluid Mech. 710, 641–658. doi:10.1017/jfm.2012.424

Day, S., Fry, R., Sakurovs, R., 2008. Swelling of Australian coals in supercritical CO2. Int. J. Coal Geol. 74, 41–52. doi:10.1016/j.coal.2007.09.006

Dicker, A.I., Smits, R.M., 1988. A Practical Approach for Determining Permeability From Laboratory Pressure-Pulse Decay Measurements. SPE Int. Meet. Pet. Eng. doi:10.2118/23312-MS

Dos Santos Amorim, E.P., Goldfeld, P., Dickstein, F., Dos Santos, R.W., Xavier, C.R., 2010. Automatic history matching in petroleum reservoirs using the TSVD method. Int. Conf. Comput. Sci. Its Appl. 6017 LNCS, 475–487. doi:10.1007/978-3-642-12165-4-38

Fathi, E., Tinni, A., Akkutlu, I.Y., 2012. Correction to Klinkenberg slip theory for gas flow in

nano-capillaries. Int. J. Coal Geol. 103, 51–59. doi:10.1016/j.coal.2012.06.008

Finsterle, S., Persoff, P., 1997. Determining permeability of tight rock samples using inverse modeling. Water Resour. Res. 33, 1803–1811.

Haskett, S.E., Narahara, G.M., Holditch, S.A., 1988. A method for simultaneous determination of permeability and porosity in low-permeability cores. SPE Form. Eval. 3, 651–658.

Hsieh, P.A., Tracy, J. V., Neuzil, C.E., Bredehoeft, J.D., Silliman, S.E., 1981. A transient laboratory method for determining the hydraulic properties of "tight" rocks-I. Theory. Int. J. Rock Mech. Min. Sci. Geomech. Abstr. 18, 245–252. doi:10.1016/0148-9062(81)90979-7

Javadpour, F., 2009. Nanopores and apparent permeability of gas flow in mudrocks (shales and siltstone). J. Can. Pet. Technol. 48, 16–21. doi:10.2118/09-08-16-DA

Javadpour, F., Fisher, D., Unsworth, M., 2007. Nanoscale Gas Flow in Shale Gas Sediments. J. Can. Pet. Technol. 46. doi:10.2118/07-10-06

Jiang, J., Younis, R.M., 2015. Numerical study of complex fracture geometries for unconventional gas reservoirs using a discrete fracture-matrix model. J. Nat. Gas Sci. Eng. 26, 1174–1186. doi:10.1016/j.jngse.2015.08.013

Jones, S.C., 1997. A Technique for Faster Pulse-Decay Permeability Measurements in Tight Rocks. SPE Form. Eval. 12, 19–26. doi:10.2118/28450-PA

Kelemen, S.R., Kwiatek, L.M., 2009. Physical properties of selected block Argonne Premium bituminous coal related to CO2, CH4, and N2 adsorption. Int. J. Coal Geol. 77, 2–9. doi:10.1016/j.coal.2008.05.020

Klinkenberg, L.J., 1941. The permeability of porous media to liquids and gases. Drill. Prod. Pract. Am. Pet. Inst. 200–213.

Kumar, H., Elsworth, D., Mathews, J.P., Marone, C., 2016. Permeability evolution in sorbing media: Analogies between organic-rich shale and coal. Geofluids 16, 43–55. doi:10.1111/gfl.12135

Levine, J.R., 1996. Model study of the influence of matrix shrinkage on absolute permeability of coal bed reservoirs. Geol. Soc. London, Spec. Publ. 109, 197–212. doi:10.1144/GSL.SP.1996.109.01.14

Li, J., Liu, D., Yao, Y., Cai, Y., Chen, Y., 2013. Evaluation and modeling of gas permeability changes in anthracite coals. Fuel 111, 606–612. doi:10.1016/j.fuel.2013.03.063

Lin, W., 1977. Compressibility fluid flow through rocks of variable permeability. Univ. Calif.

Liu, S., Harpalani, S., 2013a. A new theoretical approach to model sorption-induced coal shrinkage or swelling. Am. Assoc. Pet. Geol. Bull. 97, 1033–1049. doi:10.1306/12181212061

Liu, S., Harpalani, S., 2013b. Permeability prediction of coalbed methane reservoirs during primary depletion. Int. J. Coal Geol. 113, 1–10. doi:10.1016/j.coal.2013.03.010

Mazumder, S., Wolf, K.H., 2008. Differential swelling and permeability change of coal in response to CO2 injection for ECBM. Int. J. Coal Geol. 74, 123–138. doi:10.1016/j.coal.2007.11.001

Metwally, Y.M., Sondergeld, C.H., 2011. Measuring low permeabilities of gas-sands and shales using a pressure transmission technique. Int. J. Rock Mech. Min. Sci. 48, 1135–1144. doi:10.1016/j.ijrmms.2011.08.004

Moore, T.A., 2012. Coalbed methane: A review. Int. J. Coal Geol. 101, 36–81. doi:10.1016/j.coal.2012.05.011

Morse, D.G., Demir, I., 2007. Resource Assessment and Production Testing for Coalbed Methane in Illinois. Illinois State Geol. Surv.

Nelson, P.H., 1994. Permeability-porosity relationships in sedimentary rocks. Log Anal. 35, 38–62.

Palmer, I., Mansoori, J., 1998. How Permeability Depends on Stress and Pore Pressure in

Coalbeds: A New Model. SPE Reserv. Eval. Eng. 539–544. doi:10.2118/52607-PA

Pan, Z., Connell, L.D., 2012. Modelling permeability for coal reservoirs: A review of analytical models and testing data. Int. J. Coal Geol. 92, 1–44. doi:10.1016/j.coal.2011.12.009

Pan, Z., Connell, L.D., 2007. A theoretical model for gas adsorption-induced coal swelling. Int. J. Coal Geol. 69, 243–252. doi:10.1016/j.coal.2006.04.006

Randolph, P.L., Soeder, D.J., Chowdiah, P., 1984. Porosity and permeability of tight sands. SPE Unconv. Gas Recover. Symp.

Rodvelt, G.D., Oestreich, R.G., 2005. Case History : First Commercial Illinois Coalbed Methane Project Commences Through a S tructured Resource Evaluation Plan. 2005 SPE East. Reg. Meet.

Shi, J.-Q., Durucan, S., 2005. A model for changes in coalbed permeability during primary and enhanced methane recovery. SPE Reserv. Eval. Eng. 8, 291–299. doi:10.2118/87230-PA

Tedesco, S., 2003. Coalbed Methane Potential and Activity of the Illinois Basin. Search Discov.

Wang, S., Elsworth, D., Liu, J., 2011. Permeability evolution in fractured coal: The roles of fracture geometry and water-content. Int. J. Coal Geol. 87, 13–25. doi:10.1016/j.coal.2011.04.009

Wang, Y., Liu, S., Elsworth, D., 2015. Laboratory investigations of gas flow behaviors in tight anthracite and evaluation of different pulse-decay methods on permeability estimation. Int. J. Coal Geol. 149, 118–128. doi:10.1016/j.coal.2015.07.009

Yamada, S.E., Jones, A.H., 1980. A review of a pulse technique for permeability measurements. Soc. Pet. Eng. J. 20, 357–358.

Zoback, M.D., Kovescek, A.R., Wilcox, J., 2013. Interdisciplinary Investigation of CO2 Sequestration in Depleted Shale Gas Formations. Lel. Stanford Jr. Univ.